Raman manipulation between momentum state components of ultracold erbium atoms

Pedro Castro Perez

Masterarbeit in Physik
angefertigt im Institut für Angewandte Physik

vorgelegt der
Mathematisch-Naturwissenschaftlichen Fakultät
der
Rheinischen Friedrich-Wilhelms-Universität
Bonn

Juli 2021

I hereby declare that this thesis was formulated by myself and that no sources or tools other than those cited were used.

Bonn, ...
           Date   Signature

1. Gutachter: Prof. Dr. Martin Weitz
2. Gutachter: Prof. Dr. Sebastian Hofferberth

Contents

iv

Introduction

Following the theory work on quantum statistics of massless integer spin particles by Raman Nath Bose in 1924 [1]. Albert Einstein predicted shortly afterwards a condensation of massive integer spin particles into the ground state at low temperatures [2, 3]. This new state of matter was later called Bose-Einstein condensation and was obtained experimentally more than 70 years later. The first Bose-Einstein condensates (BECs) were generated in 1995 by several research groups for three different chemical elements: rubidium [4], sodium [5] and lithium [6]. The following years lead to a rising interest of this exotic state of matter due to their quantum properties that allow to describe the system of particles by using just the coherent wave function of a single-particle. Due to this, BECs for many other elements were achieved. Some examples are: alkali metals like strontium [7], and Lanthanides like ytterbium [8], dysprosium [9] and erbium [10]. Even in non-atomic bosonic particles like photons [11].

Nowadays, there has been increasing interest in the condensation of atoms belonging to the lanthanide group. This is due to two main reasons: the first one being the large magnetic moment that these elements normally have, which increases the effect of dipole-dipole interaction [10, 12]. The second reason will be more relevant for this experiment and is based on the fact that these atoms normally have a non-vanishing electronic angular momentum in their energetic ground state. For the case of erbium, the orbital angular momentum has a value of $L = 5$ for the ground state. This allows to use Raman transitions between Zeeman sublevels of the ground state in the fine structure scheme. Increasing the available detuning ranges, which enables the possibility of using large values for the detuning. This reduces the photon scattering rates and increases the coherence times for the BEC [13].

Raman manipulation permits the use of a method called phase imprinting, which generates synthetic magnetic fields and have been theorised to be achievable with lanthanide atoms [14]. If these synthetic fields were generated with enough strength, it would enable the fractional quantum Hall regime for neutral atoms. This could have major implications possibly enabling studies of topological quantum computation. The synthetic magnetic fields have already been observed as vortices structures inside the BEC for rubidium [15]. However, the strength of these fields was limited by the coherence time using the available transitions in this element. As said, the use of erbium is expected to allow for longer coherence times, which could generate larger synthetic magnetic fields and possibly enable the fractional quantum Hall regime for a cold atom ensemble. In order to achieve the Raman manipulation process required, the starting point for this work will be the generation of an erbium (Er^{168}) Bose-Einstein condensate (BEC) with an approximate atom number of 50000.

This thesis aims to study a Raman manipulation set-up formed by two counter-propagating beams detuned with respect to an erbium transition near 841 nm. The main part will consists of the characterisation of Raman transitions between momentum states for the energetic ground state of erbium. This corresponds to the atomic BEC diffraction with the Raman beams forming and optical lattice. The resulting effect is the generation of different momentum orders, similar to the well-known process of light diffraction. After this, the main focus will be on the achievement of Raman transitions into the spin-momentum configuration between different sublevels, generated by Zeeman splitting of the ground energy level of the erbium BEC. This achievement represents the ground work for the future realisation of strong enough synthetic fields to reach the fractional quantum Hall regime for an atomic physics system. However, in order to obtain the Raman manipulation of internal spin states, an additional experiment with radio frequency (RF) transitions is required. Its main purpose is to characterise and prepare the magnetic fields causing the Zeeman splitting of the ground state.

Therefore, the thesis it is divided in different chapters according to its content. Chapter 2 shows the properties of erbium, introduces the basic theory of an atomic BEC and briefly describes the experimental set-up used to achieve and measure an erbium BEC. Chapter 3 gives the theoretical basis for the diffraction of a BEC with an optical lattice. Chapter 4 describes the RF transitions experiment together with a basis of the Raman manipulation of the spin-momentum space. Chapter 5 shows the measured and analysed results. And finally, 6 serves as a conclusion and outlook to the thesis.

Atomic erbium Bose-Einstein condensate

This chapter has the objective of briefly review some relevant properties of Erbium, which will clarify what makes it relevant in the study of ultracold atoms. After this, the basic theory of Bose-Einstein condensation will be discussed, along with a brief description of the experimental phases required to create and observe an erbium BEC. This experimental realisation will be the foundation on which the following chapters will be grounded when discussing further experimental achievements.

2.1 Properties of atomic erbium

Erbium is a chemical element with an atomic number of 68, which belongs to the series of Lanthanides. It is also part of the group called rare-earth elements and it was first discovered by G. Monsander in 1843 [16]. The name of "Erbium" comes from the name of the Swedish village of Ytterby, the place where it was extracted. At that time, the similarity of rare-earth metals' chemical properties made their distinction extremely difficult. For this reason, what G. Monsander thought to be pure Erbium oxide was in fact a mixture of different rare-earth metal oxides. The element is not obtained in a reasonably pure form until 1937 by W. Klemm and H. Bommer [17].

Considering some basic properties of this element, under standard conditions erbium is in a solid state. It has a silver shining surface, which oxidises with air contact. This rare-earth metal has a melting point of $1\,802\,$K and boiling point of $3\,136\,$K. As a result, to be able to work with a free atomic gas of erbium requires to heat up the solid metal of erbium to high temperatures [18].

The number of stables erbium isotopes is 6 , which are given in Table 2.1. All of them are bosons with nuclear spin of zero, in exception of ^{167}Er, which is a fermion with nuclear spin of 7/2. The chosen isotope for this experiment is ^{168}Er because of its bosonic nature (see Section 2.2), high abundance and favourable scattering properties [19].

In addition to these properties, erbium atoms have a rather complex energetic level scheme due to its open 4f shell. This one lacks 2 electrons to be completely filled, which makes erbium to have an electronic ground state with an orbital angular momentum value of $L = 5$ and a magnetic moment of seven Bohr magneton $7\mu_B$ [20]. This high value for the orbital angular momentum in the ground state of erbium provides advantages for Raman-coupling processes. The main one is a wider range for the detuning from atomic resonance, which allows for longer coherence times and thus, stronger synthetic magnetic fields when comparing with alkali metals like rubidium or caesium, commonly used in ultracold atoms experiments [14].

Isotope	Abundance [%]	Atomic Mass [u]	Nuclear Spin [$\hbar$]
Er^{162}	0.14	161.928775	0
Er^{164}	1.61	163.929198	0
Er^{166}	33.60	165.930290	0
Er^{167}	22.95	166.932046	7/2
Er^{168}	26.80	167.932368	0
Er^{170}	14.90	169.935461	0

Table 2.1: Table with the stable isotopes of Erbium that can be found on Nature with their respective Abundance ratio, Atomic mass and Nuclear Spin. Spectroscopy data taken from [21].

A scheme of erbium energy levels together with the atomic transitions used in this experiment can be seen in figure 2.1. The scheme shows that the electronic ground state of erbium is [Xe] $4f^{12}6s^2$, where [Xe] represents the complete electronic configuration of Xenon[1]. Moreover, the used optical transitions are represented by coloured arrows in the figure and its spectroscopic data is shown in table 2.2. From now on, these three transitions will respectively be referred to as the 401nm, 583nm, and 841nm transitions.

Parameters			Transitions		
Name	Symbol	Unit	401nm	583nm	841nm
Wavelength in vacuum	λ	nm	400.91	582.84	841.22
Lifetime	τ	µs	0.045	0.857	20
Natural linewidth	$\Delta\nu_0$	kHz	33 370	185.71	7.96
Decay rate	Γ	s^{-1}	2.22×10^8	1.17×10^6	5.00×10^4
Saturation intensity	I_S	mW cm^{-1}	71.80	0.12	0.00172
Doppler temperature	T_D	µK	848.69	4.46	0.19
Doppler velocity	v_D	cm s^{-1}	21.5	1.49	0.31
Recoil temperature	T_R	nK	354.95	167.94	80.43
Recoil velocity	v_R	mm s^{-1}	5.93	4.08	2.82

Table 2.2: Spectroscopic data for the optical transitions of Erbium used in this experiment. These transitions are called the 401nm, 583nm, and 841nm transitions and can be seen in figure 2.1. Shown spectroscopic data taken from [20, 22–25]

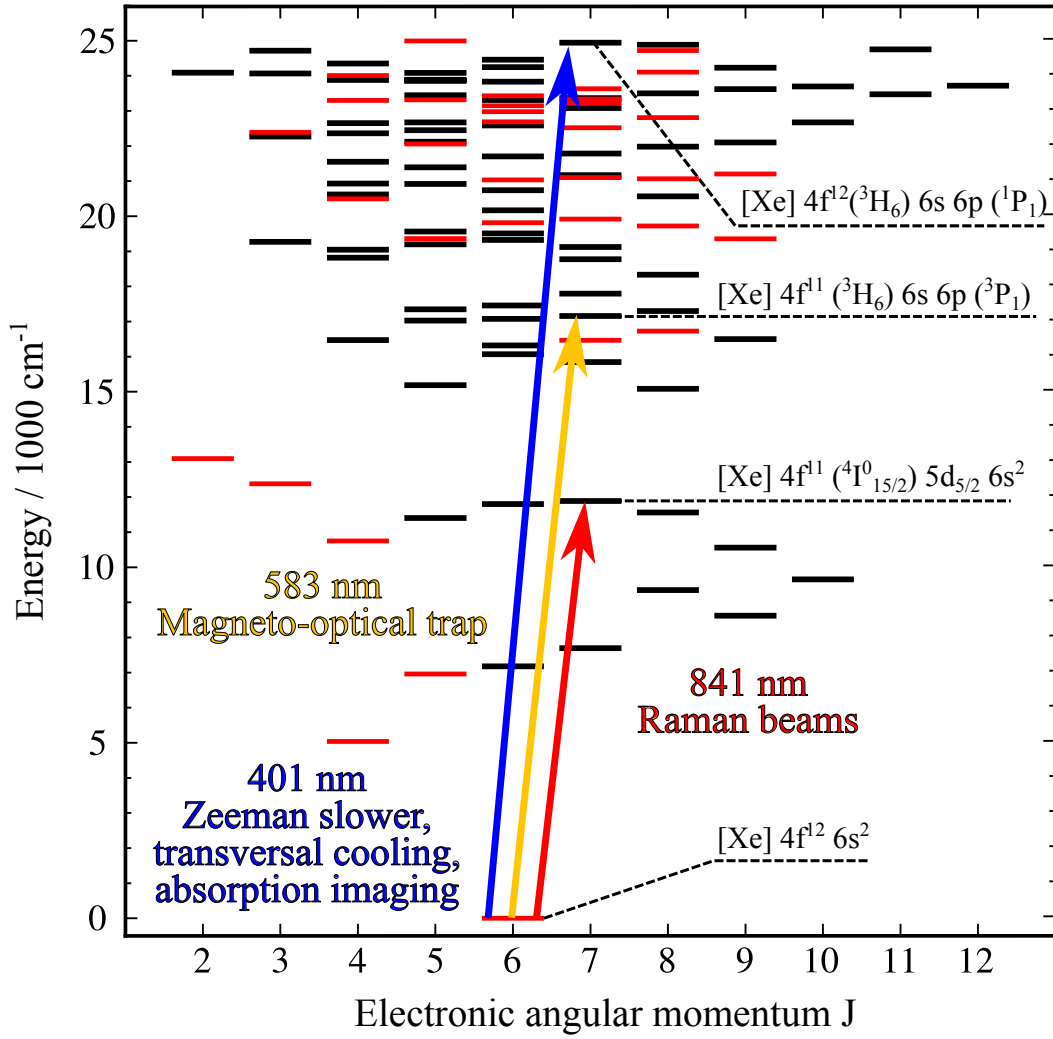[1] [Xe] = $1s^2\ 2s^2\ 2p^6\ 3s^2\ 3p^6\ 3d^{10}\ 4s^2\ 4p^6\ 4d^{10}\ 5s^2\ 5p^6$

Figure 2.1: Energy level scheme of Erbium represented as a function of the total angular momentum J. This scheme shows only a range of energies relevant for the experiment of up to 25000 cm^{-1}. The different arrows show the used transitions and for which phase of the experiment they are used for. The red lines represent energy states with even parity and the black lines those with odd parity. Data taken from [26].

2.2 Bose-Einstein condensation

A Bose-Einstein condensate (BEC) can be defined as a state of matter formed when a sufficiently dense gas of bosons occupy macroscopically the energetic ground state. To understand this definition and the next theoretical principles, it is necessary to explain what is a Boson. In quantum mechanics, bosons are defined as particles with an integer value in their spin. This characteristic makes them have a symmetric wave function under the interchange of two particles, which allows multiple bosons in a given system to be in the same quantum state. Unlike the counterpart fermions, particles counting with a half odd integer spin and an anti-symmetric wave function. This case leads to Pauli's exclusion

principle that avoids more than one fermion to occupy the same quantum state [27].

It was the Indian physicist S. N. Bose in 1924, the first one who described in a successful way an ideal gas of non interacting free photons, behaving like mass-less bosons. His idea was initially rejected for publication in scientific journals. However, Bose sent the manuscript to A. Einstein, who recognized its importance, translated the paper to German and saw to it that was published [1]. After this, Einstein extended Bose's treatment to massive particles and predicted the occurrence of a phase transition in a gas of non-interacting atoms, what is today known as a BEC [2, 3].

These publications led to Bose-Einstein statistics, a model that explains the energetic behaviour of a non-interacting gas of indistinguishable N bosons, each one with mass M [28, 29]. The average number of particles at a given non-degenerate state with wave vector $\mathbf{k}$ and energy $E_{\mathbf{k}} = \hbar^2 \mathbf{k}^2 / 2M$ is given by

$$\bar{N}_{\mathbf{k}} = \frac{1}{e^{(E_{\mathbf{k}} - \mu)/k_B T} - 1}, \tag{2.1}$$

for an ideal gas of bosons in thermal equilibrium at a temperature T, Boltzmann constant k_B and chemical potential μ, which depends of N and T [28]. The total number of particles in all energy states is expressed as

$$N = \sum_{\mathbf{k}} \frac{1}{e^{(E_{\mathbf{k}} - \mu)/k_B T} - 1}. \tag{2.2}$$

So the chemical potential μ is determined such that Eq. (2.2) is satisfied for any given N remaining constant. Now, expanding into the thermodynamic limit where N and the occupied volume V are increased to infinite values keeping the particle density $n = V/N$ constant. The sum over $\mathbf{k}$ appearing in Eq. (2.2) can be replaced by an integral such as

$$n = \frac{N}{V} = \frac{1}{(2\pi)^3} \int d^3k \frac{1}{e^{(E_{\mathbf{k}} - \mu)/k_B T} - 1}. \tag{2.3}$$

For decreasing values of T and constant n, the chemical potential increases becoming zero at a critical temperature T_C. By making $\mu = 0$, $T = T_C$ and $E_{\mathbf{k}} = \hbar^2 \mathbf{k}^2 / 2M$ in Eq. (2.3) results

$$n = \zeta(3/2) \left(\frac{M k_B T_C}{2\pi \hbar^2} \right)^{3/2}, \tag{2.4}$$

where $\zeta(3/2) \simeq 2.612$ denotes the Riemann zeta function evaluated at 3/2. So the critical temperature of the BEC is given by

$$T_C = 3.31 \frac{\hbar^2 n^{2/3}}{k_B M}. \tag{2.5}$$

A relevant case of study is when $T < T_C$ because a fraction of the N bosons remains in the ground state with an energy $E = 0$. So the ideal gas of bosons can be divided in two energetic groups $N = N_{E=0} + N_{E>0}$. It must be noted that, the replacement of a sum by an integral in Eq. (2.3) can only be take place in group of particles with an energy greater than zero $E > 0$. As a result of this, the integral of Eq. (2.3) for the case $T < T_C$ results

$$\frac{N_{E>0}}{V} = \zeta(3/2)\left(\frac{Mk_BT}{2\pi\hbar^2}\right)^{3/2}. \qquad (2.6)$$

Using now equations (2.5), (2.4) and the fact that $N_{E>0} = N - N_{E=0}$ results in an expression of the relative population of a BEC in an ideal bosons gas as a function of temperature:

$$\frac{N_{E=0}}{N} = 1 - \left(\frac{T}{T_C}\right)^{3/2}. \qquad (2.7)$$

An intuitive way to think about this is to imagine the bosons as wave packets with a size of the thermal de Broglie length λ_{th}. This parameter is conventionally defined [30].

$$\lambda_{th} = \frac{h}{\sqrt{2\pi Mk_BT}}. \qquad (2.8)$$

For falling temperatures, the thermal de Broglie length begins to increase and the wave packets representing the bosons become greater in size. At $T \lesssim T_C$ the particles begin to occupy macroscopically the ground state and its wave packets start to overlap forming a macroscopic wave function, capable of describing the whole particle system. This is one of the most relevant properties of a BEC. Now, we combine equations 2.4 and 2.8 to obtain for a squared well potential the critical value

$$n\lambda_{th}^3 = \zeta(3/2) \simeq 2.612 \qquad \text{for } T = T_C. \qquad (2.9)$$

This product of density with cubic de Broglie length is defined in the literature as phase-space density $\rho_{psd} \equiv n\lambda_{th}^3$. It is normally used as a parameter that helps to quantify any given bosonic system. From Eq. (2.9), one can deduce that to form a BEC with an atomic (bosonic) cloud in three dimensions the phase space density must fulfil $\rho_{psd} \geq 2.612$. As a result, the required conditions to form a BEC can only be fulfilled when the atomic cloud is sufficiently cold and dense. For the case of a three dimensional gas of atoms trapped in an harmonic potential this condition over the phase space density decreases to $\rho_{psd} \geq 1.2$ [29].

A further description about the theory of Bose-Einstein Condensation can be found in [28, 29].

2.3 Experimental realization of an erbium BEC

The generation of an erbium BEC requires a multiple set of experimental phases, with each one based on different physical principles. The main purpose of this section is to discuss briefly every one of those together with its underlying foundation. For a more detailed description of the experimental set refer to [31].

Figure 2.2 shows a scheme of the experimental setup. It must be noted that all the devices used for the experiment lay on top of three optical tables represented in the figure by grey areas. Moreover, the laser beams produced by different laser systems are represented by coloured lines. The erbium atoms are at all times kept inside an ultra-high vacuum (UHV) system formed by an oven, Zeeman slower (ZS) and main chamber. This UHV is maintained by two ion getter pumps reaching a pressure of 10^{-8} mbar. Additionally, for the main chamber there is a titanium sublimation pump, which reduces the vacuum even further to 10^{-10} mbar. The need of an UHV comes from the fact that to reach an

atomic BEC, the cooling process must be so extreme that any interaction with room temperature atoms would lead to heating and destruction of the cold erbium cloud.

Most of the laser systems in this experiment produce resonant light for the ^{168}Er atomic transitions. For this reason, these light sources are kept on different optical tables separated from the UHV system. This reduces unwanted atom-light interaction that could decrease the cooling capabilities of the experiment is reduced. This laser light is guided into the main table by using optical fibres that can be blocked and unblocked through the use of mechanical shutters and acousto-optic modulators (AOMs) before the fibre coupler. Allowing for a fast response time (typically a few hundreds nanoseconds) and better control of the experimental phases.

The different phases required to obtain an erbium BEC are chronologically very organized. There is almost no temporal overlay between phases. This allows for a very accurate description of the experiment by just explaining every procedure in a chronological order. In every cycle, the atoms start in the oven and pass through the transversal cooling (TC) and zeeman slower (ZS) to reach the main chamber, where the magneto-optical trap (MOT), optical dipole trap (ODT) and evaporative cooling take place to generate the erbium Bose-Einstein condensate.
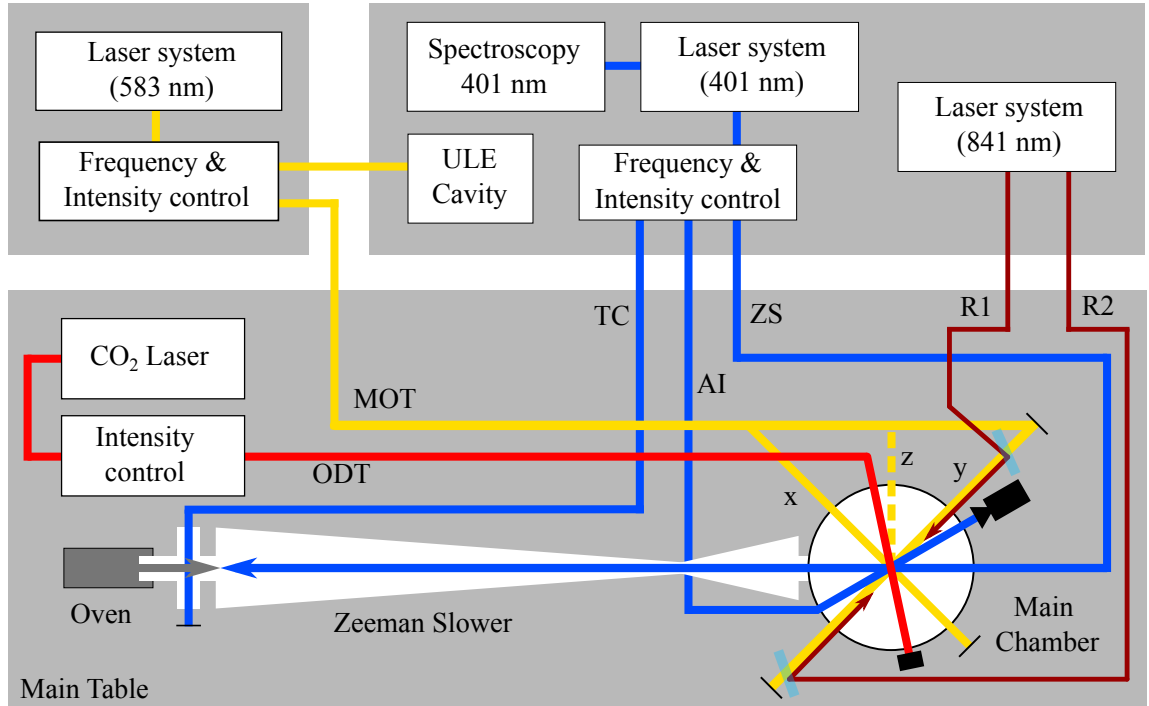

Figure 2.2: Scheme of the experimental setup. It is divided in three optical tables represented by grey areas. The 401nm laser system is used for the transversal cooling (TC), zeeman slower (ZS) and absorption imaging (AI). It is generated by a frequency doubled diode laser locked to a spectroscopic signal of the 401nm transition of ^{168}Er. The 583nm laser system is used for the magneto-optical trap (MOT) and is frequency looked to an ultra low expansion cavity (ULE cavity). This trap uses 401nm laser beam in three spacial dimensions x, y and z. The CO_2 laser is used as main source of an optical dipole trap (ODT). The 841nm laser system is used to form the two lattice beams used for Raman transition processes which will be described in Chapters 3 and 4.

.

2.3.1 Oven

The required first step to form an erbium BEC consist in transforming the solid state metal of erbium into an atomic beam. In order to achieve this, an oven of the type known as Dual filament effusion cell (DFC)[2] is used, operating inside an UHV chamber. The left side of Figure 2.3 shows a basic scheme of this device, which is divided into two tantalum wired cavities. The first one is called Effusion cell (EC) and contains the bulk metal of erbium, which is heated up to 1 200 °C and sublimated into gas. After this, the erbium gas is transferred through a 3 mm pinhole into the second cavity of the DFC known as Hot lip (HL). This last part of the oven is heated a 100 °C higher than the EC temperature to avoid condensation of material at the pinholes. Lastly, the erbium gas leaves the oven forming an atomic beam through a second pinhole that connects the HL cavity with the rest of the vacuum system. The speed at which the atoms are leaving the oven can be estimated in average with a parameter called root mean squared (RMS) velocity $\bar{v}_{\mathrm{RMS}}$. For the case of an ideal gas it has been obtained as [32]

$$\bar{v}_{\mathrm{RMS}} = \sqrt{\frac{3k_B T}{M}}. \tag{2.10}$$

This means that for a HL temperature of 1 300 °C the resulting RMS velocity of the erbium beam leaving the oven is approximately 483 m s^{-1}.
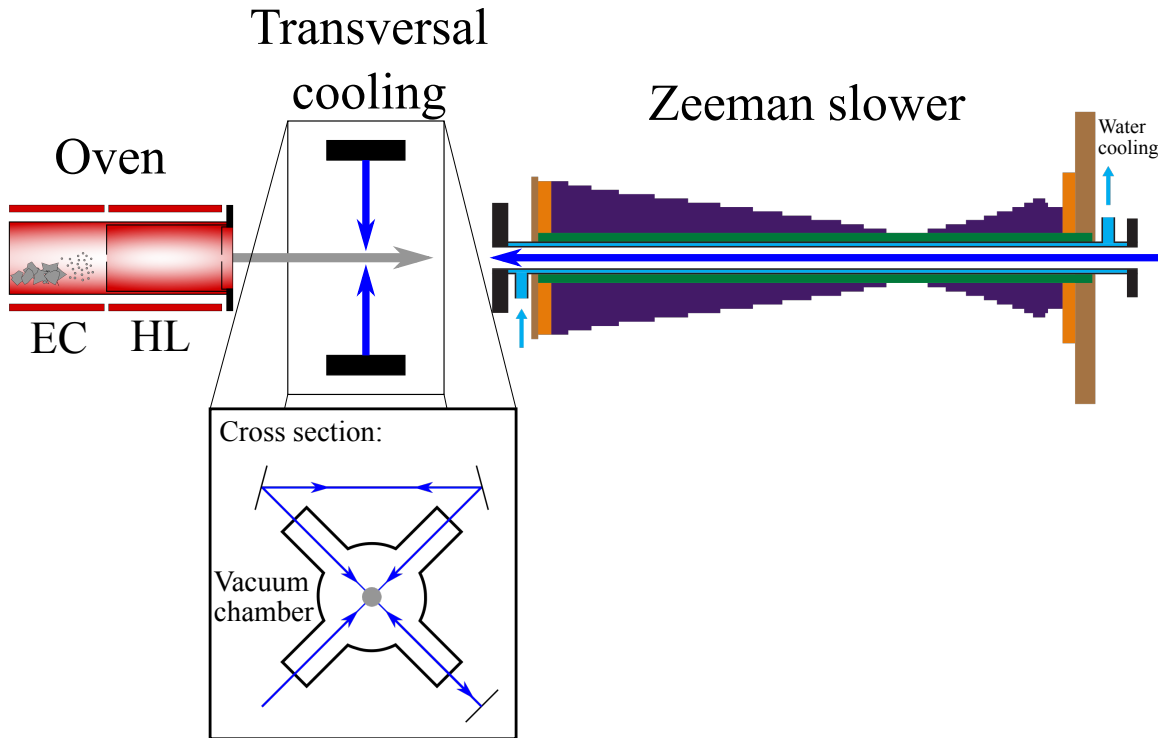

Figure 2.3: Scheme of the oven, transversal cooling and zeeman slower. The atomic beam of erbium and the 401 nm laser beam are represented by grey and blue arrows respectively. A cross section of the transversal cooling can be seen inside a box. And the different coils used for the zeeman slower are also represented.

---

[2] Model DFC-40-10-WK-2B by CreaTec Fischer & Co. GmbH

2.3.2 Transversal and laser cooling

The atomic beam produced by the DFC oven presents two main problems, for the generation of an atomic BEC. These are a poor collimation of the beam and a high speed of the erbium atoms forming the beam. These obstacles must be addressed in order to increase the atomic flux at the atomic ensemble position and form an erbium BEC. The main purpose of this transversal cooling (TC) phase is to solve the problem due to poor beam collimation. While the high atomic speed problem will be dealt with in the following Zeeman slower section. However, these two phases are based in the same underlying physical principle, commonly known as laser cooling.

Laser cooling

This technique relies on the force applied on particles by red-detuned near resonant photons. From Equation (2.10), it can be seen that the temperature of an ideal gas is proportional to its velocity. So this light-produced force, known as radiation pressure, can be used as a way to lower the temperature of an atomic gas simply by reducing its overall speed. To gain an insight into the physical behaviour of this force, it is necessary to consider a two-level atomic system [33]. This two level atom has a ground state $|g\rangle$, an excited state $|e\rangle$ and an energy difference between both states of $\Delta E = \hbar\omega_0$, where ω_0 represents the atomic resonance frequency. The atom at rest can absorb a photon with resonant frequency ω_0. Thus, transferring its energy $\hbar\omega_0$ and momentum $\vec{p} = \hbar\vec{k}$ to the atom. Where $\vec{k}$ represents the photon wave vector, such as for light with wavelength λ, the wave number results $|\vec{k}| = 2\pi/\lambda$. From the interaction between an atom moving with velocity $\vec{v}$ and a beam light with wave vector $\vec{k}$, the force experienced by the atom is called radiation pressure force and has the following expression [33]

$$\vec{F} = \frac{\hbar\vec{k}\Gamma}{2} \frac{s_0}{1 + s_0 + \left(\frac{2(\delta - \vec{k}\vec{v})}{\Gamma}\right)^2},$$

(2.11)

where $\Gamma = 1/\tau$ is the decay rate, $\delta = \omega - \omega_0$ the detuning between laser light and atomic resonance frequency and $s_0 = I/I_s$ the saturation parameter defined as the ratio of laser light intensity I and saturation intensity $I_s = 2\pi^2\hbar c/3\lambda^2\tau$, with λ the light wavelength and c the speed of light. This equation for the radiation pressure suggests that a beam of atoms can be slowed down by a red-detuned ($\delta < 0$) counter-propagating optical beam. And therefore, the atomic beam temperature can decrease by following Equation (2.10). However, this cooling process presents some limitations because of the spontaneous emission effects. The process taking place produces spontaneous emission of photons by the atom with a vanishing momentum transfer, but its mean squared value does not vanish and heats up the atoms. For a limiting case in which this heating effect equals the optical cooling, an equilibrium temperature is reached known as Doppler limit or Doppler temperature

$$T_D = \frac{\hbar\Gamma}{2k_B},$$

(2.12)

which is a theoretical temperature limit for an ideal two levels atom [33]. It can be seen from Equations (2.11) and (2.12), that there must be a trade off in the experimental value for decay rate of the excited level Γ. In order to achieve a strong enough value for the radiation pressure at the same time that a low enough Doppler temperature. There is however, the capability of cooling down further than the Doppler limit with the use of more refined techniques for multilevel atoms, such as the polarization

gradient cooling approach [34].

Transversal cooling

Through the use of optical cooling this experimental phase is used to collimate the atomic beam produced by the DFC oven. In Figure 2.3, a scheme and cross section of the TC can be seen. The main objective is to increase the flux of atoms passing from DFC to the initial part of the ZS aperture. To achieve this, a crossed optical beam of the red-detuned near 401 nm transition, transversal to the atomic beam, is used. As seen in the cross section scheme, the optical cross beam is overlaid with an ingoing and outgoing part. This results in four optical beams traversing the atomic beam in four perpendicular directions. This scheme together with the optical force described Equation 2.11 leads to radiation pressure acting towards the atomic beam centre, collimating it. Moreover, the high value for the decay rate of $\Gamma = 2.22 \times 10^8 \, \mathrm{s}^{-1}$ for the 401 nm transition (see Table 2.2) makes the radiation pressure force considerably strong. In order to enhance the interaction between atomic and light beam, this last one has its shape widened elliptically with the mayor axis parallel to the atomic beam.

2.3.3 Zeeman slower

As it has already been discussed in the previous section, the second problem that arises is the high speed at which the atomic beam is travelling. At the end of Section 2.3.1, a calculation of the average speed of atoms leaving the oven resulted in approximately $457 \, \mathrm{m \, s}^{-1}$. However, it has been estimated that the maximal trapping velocity is a few meters per second, for the specific magneto-optical trap used in this experiment [31]. The main objective of this experimental phase is to reduce the average atomic speed so that it is feasible to trap the atoms inside an atomic cloud. This requires another red-detuned laser beam from the near 401 nm transition moving in the opposite direction of the atomic beam. A counter-propagating optical beam transmits radiative pressure to the atomic beam as seen in Equation (2.11). However, as the atomic beam begins to be slowed down, the average velocity of the atoms $\vec{v}$ is reduced and the Doppler shift value $\Delta\omega_D = -\vec{k}\vec{v}$ in Equation (2.11) also decreases. This results in a change of the resonance condition and suppression of the radiative pressure, which reduces the slowing effect of the atomic beam. In order to avoid this, the inner splinting of the atomic energy levels must be changed with the use of an spatially varying magnetic field. Thus, at the same time that the beam is being slowed down, the effective atomic resonance is being changed to match a reduction of the Doppler shift $\Delta\omega_D$. The atomic energy shift is affected by the position-dependent magnetic field $\vec{B}$, where the dominant effect is called Zeeman splitting $\Delta\omega_Z$, given by [35]

$$\Delta\omega_Z = \frac{\mu_{\mathrm{eff}}}{\hbar}|\vec{B}|, \tag{2.13}$$

where μ_{eff} represents the effective magnetic moment [33]. The required condition is that Zeeman and Doppler shifts compensate each other $\omega_Z = -\omega_D$. For this to be achieved, the required magnetic field as function of the position z in the axis where the atomic beam is moving can be expressed as

$$|\vec{B}(z)| = \frac{\hbar k}{\mu_{\mathrm{eff}}}\sqrt{v_0^2 + 2a(z - z_0)}, \tag{2.14}$$

with a being the deceleration parameter, v_0 the maximal velocity at which the atoms can be slowed down and z_0 the spacial point where the atom deceleration begins. These types of magnetic fields

can be shaped using coils with a spatial dependent number of wires, which is the case for a common zeeman slower (ZS) like the one used in this experiment. Figure 2.3 shows a scheme of the ZS with a counter propagating beam tuned to near the 401 nm transition providing the radiation pressure to the atomic beam and a group of five independent coils providing the magnetic field described by Equation (2.14). For more details on the ZS experimental set-up and the description of these coils refer to [36].

2.3.4 Magneto-optical trap

Once the atomic beam has passed the ZS and has been slowed down to a few meters per second, the erbium atoms enter the main UHV chamber shown in Figure 2.4. The next step requires trapping the atoms in a local region of the main chamber with the use of a Magneto-optical trap (MOT). Thus, the atomic beam forms an ensemble of atoms with an even lower average velocity, which means a reduction in the erbium atoms temperature within the ensemble.

In this case, the MOT consists of three counter-propagating laser beam pairs, red-detuned to the near 583 nm transition. Each of these beam pairs is perpendicular to the other two, forming three spatial axes inside the main chamber (x, y and z) with an overlay region where the atomic ensemble will be made. In addition to this, two water cooled coils in an anti-Helmholtz configuration are required to create a quadrupole magnetic field, which is zero in the centre of the region formed by the six laser beams overlay. The result of this magneto-optical set up is the generation of a three dimensional spatially dependent restoring force, which binds the erbium atoms to remain inside the overlaying region. To have a physical interpretation of why this is happening, it is necessary to consider a two level atom located inside this region. Due to spatial symmetry and to simplify things even further, just effects in the z axis will be considered. Because of Zeeman splitting, the magnetic field $B_z = Az$ produced by the anti-Helmholtz coils at the z direction, splits up the atomic states' degeneracies. Thus, the resulting force $\vec{F} = F\vec{e}_z$ being applied to an atom at a position z' and a speed $\vec{v} = v\vec{e}_z$ comes from Equation (2.11) applied in the two axial directions like

$$\vec{F} = \frac{\hbar\vec{k}\Gamma}{2}\frac{s_0}{1 + s_0 + \left(\frac{2\delta_+}{\Gamma}\right)^2} - \frac{\hbar\vec{k}\Gamma}{2}\frac{s_0}{1 + s_0 + \left(\frac{2\delta_-}{\Gamma}\right)^2}, \tag{2.15}$$

where

$$\delta_\pm = \delta \mp \vec{k}\vec{v} \pm \frac{\mu_{\text{eff}}B_{z'}}{\hbar}, \tag{2.16}$$

and

$$\mu_{\text{eff}} = \mu_B(g_e m_e - g_g m_g), \tag{2.17}$$

with μ_B the Bohr magneton, $g_{g/e}$ the Landé factor, $\pm\vec{k} = \pm|k|\vec{e}_z$ the wave vector of both beams and $m_{g/e}$ the quantum number of the total angular momentum. As a result of this, the atom located in z' will interact most likely with the light beam for which the detuning δ_+ or δ_- is smaller. This means that an atom moving in any direction away from the MOT will absorb only photons from the optical beams that can push it towards the MOT's centre. Because of the fact that erbium's near 583 nm transition has a narrow line-width of 185.71 kHz (see Table 2.2), the type of MOT used here is commonly known as a narrow-line MOT, which allows to achieve lower temperatures due to Equation (2.12). The experimental phase of the MOT can be divided into two main parts. The first one being known as the loading phase, where the erbium atoms are collected from the ZS by using a laser detuning

of around 30 times erbium's near 583 nm transition linewidth. And second, the compressing phase, where the ensemble of atoms inside the MOT is compressed by changing the magnetic fields and reducing the laser detuning to around 1 or 2 times the linewidth. This results in a denser, colder and more confined atomic cloud, which will be useful for the following ODT phase. The typical temperature range achieved for erbium clouds trapped in the used MOT are in the mK and µK regimes at the loading and compressing phase respectively. For a more in deep description of the underlying principles of Magneto-optical traps, or a characterization of the used set up, refer to [31, 33, 37].
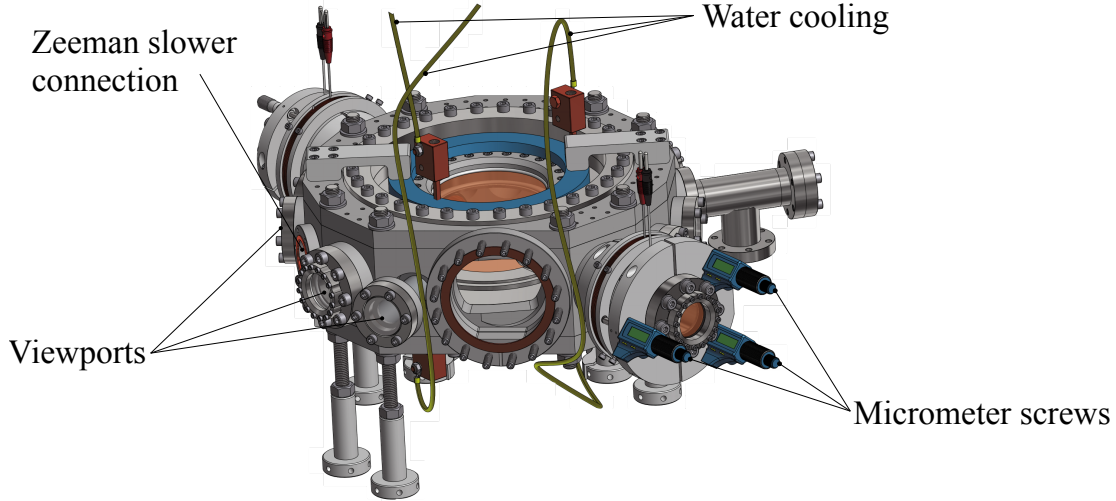

Figure 2.4: Technical drawing of the main chamber. It has 17 viewports with different diameters and each one with anti-reflection coatings for the used laser transitions. The chamber also counts with a configuration of water cooled coils inside it, and some micrometer screws connected to lenses for the collimation of different laser beams passing through the ports.

2.3.5 Optical dipole trap

As it has already been mentioned, the lowest possible temperature for the atoms trapped inside the MOT is just a few µK, which is not low enough to achieve the required critical temperature T_C given by equation (2.5). This prevents to form an erbium Bose-Einstein condensate with the use of only a magneto-optical trap. Therefore, lower temperatures of the erbium ensemble must be reached by using an additional experimental phase known as Optical dipole trap (ODT). This type of trap is achieved with the use of a CO_2 laser beam at a wavelength of 10.6 µm and a power of approximately 60 W, which is focused in a focal point with 25 µm of radius. This laser beam is aligned in a way that its focal point overlays with the region where atomic erbium is trapped inside the MOT. This way, the transference of atoms from MOT to ODT can be performed with the least possible losses in the total number of trapped atoms.

In the different types of ODTs, the one used here has the peculiarity that its CO_2 laser beam wavelength is far detuned for any erbium atomic transition like $\lambda_{ODT} \gg \lambda_0$. This type of ODT is commonly known as Quasi-electrostatic trap (QUEST) and were first proposed by T. Takekoshi et al. in 1994 [38]. Due to the far detuning between trap and atomic transitions, the trap can be approximated as a quasi-electrostatic field, which polarizes the atom and induces an atomic dipole moment [13]. The

interaction between this induced dipole $\vec{p}$ and the electric field $\vec{E}(\vec{r})$ from the CO_2 laser, is described by an interaction potential $U_{\text{dip}}(\vec{r})$ given by

$$U_{\text{dip}}(\vec{r}) = -\frac{1}{2} < \vec{p} \cdot \vec{E}(\vec{r}) >= -\frac{\text{Re}(\alpha)I(\vec{r})}{2\epsilon_0 c}, \tag{2.18}$$

here, <> denotes time average over the rapid oscillating terms, $I(\vec{r}) = 2\epsilon_0 c|\vec{E}(\vec{r})|^2$ is the laser intensity, and α the complex polarizability, such as $\vec{p} = \alpha(\omega_l) \cdot \vec{E}(\vec{r})$ with ω_l being the laser frequency. A good approximation can be obtained when considering the intensity distribution of the CO_2 laser beam as Gaussian:

$$I(\vec{r}, z) = \frac{2P}{\pi w^2(z)} e^{-2r^2/w^2(z)}. \tag{2.19}$$

The distribution is represented in cylindrical coordinates with z being the propagation direction and $\vec{r}$ the radial position. Additionally, $w(z)$ represents the beam radius and P the optical power. Using now Equations (2.18) and (2.19), the spatial behaviour of the interaction potential can be obtained as

$$U_{\text{dip}}(\vec{r}, z) = -U_0 e^{-2r^2/w^2(z)}, \tag{2.20}$$

where $U_0 = \frac{\text{Re}(\alpha)P}{\epsilon_0 c \pi w_0^2}$ is the trap depth at the focal point of the trap beam (i.e. for $\vec{r} = 0$ and $z = 0$), and $w_0 = w(0)$ the beam waist at the focal point. Considering now, the atoms trapped inside the ODT with an energy lower than the maximal trap depth, the radial and longitudinal expansions would be considerably smaller than the trap scales i.e. the beam waist w_0 and Rayleigh length $z_R = \pi w_0^2/\lambda$. This way, a Taylor expansion of $U_{\text{dip}}(\vec{r}, z)$ around the beam focal point can be performed

$$U_{\text{dip}}(\vec{r}, z) \simeq -U_0 \left[1 - 2\left(\frac{r}{w_0}\right)^2 - \left(\frac{z}{z_R}\right)^2\right]. \tag{2.21}$$

This is equivalent to the expression for an harmonic oscillator inside a cylindrical potential. By using Equation (2.21), the generated dipole force $\vec{F}_{\text{dip}}$ affecting the neutral erbium atoms can be obtained as

$$\vec{F}_{\text{dip}}(\vec{r}, z) = -\vec{\nabla} U_{\text{dip}}(\vec{r}, z) = -2U_0 \left(\frac{2r}{w_0^2}\hat{e}_r + \frac{z}{z_R^2}\hat{e}_z\right), \tag{2.22}$$

where $\hat{e}_r$ is the radial and $\hat{e}_z$ the longitudinal unitary vectors in cylindrical coordinates. This final expression shows that for atoms close enough to the trap, there is a dipole force pushing them linearly towards its centre.

2.3.6 Evaporative cooling

Once atomic erbium is trapped in an ODT, the required temperatures for achieving a BEC can not yet be reached. During the optical dipole trap phase there is another cooling technique available, commonly known as Evaporative cooling, which allows for the reaching of temperatures lower than T_C from Equation (2.5) [39]. See Figure 2.5, the physical idea behind this phase is based on the fact that a group of trapped atoms have velocities, which follow a Maxwell-Boltzmann distribution with temperature T_0 and average velocity $\bar{v}$. Because of this, the temperature of a trapped atom ensemble,

just requires letting the atoms with more energy leave the trap, while keeping the less energetic ones inside. This can be achieved by simply decreasing the laser intensity of the ODT's beam, allowing for the atoms with higher energy to leave the trap. After this, the remaining atoms, of reduced average energy, will interact via collisions with each other, restabilising the Maxwell-Boltzmann distribution and decreasing its temperature in a process called re-thermalization. For a more effective cooling, this is performed in a continuous way and the speed at which the intensity is decreased becomes very important. Too fast would prevent the atoms from re-thermalizing and too slow would lead to problems with the maximum holding time of the trap. Any of both cases results in is inefficiency of the cooling process and the lost of too many atoms required to form a BEC. For more details on evaporative cooling refer to [31, 33, 37]. The typical value reached for an erbium BEC are a number of around 30 000-60 000 atoms at temperature below 200 nK.
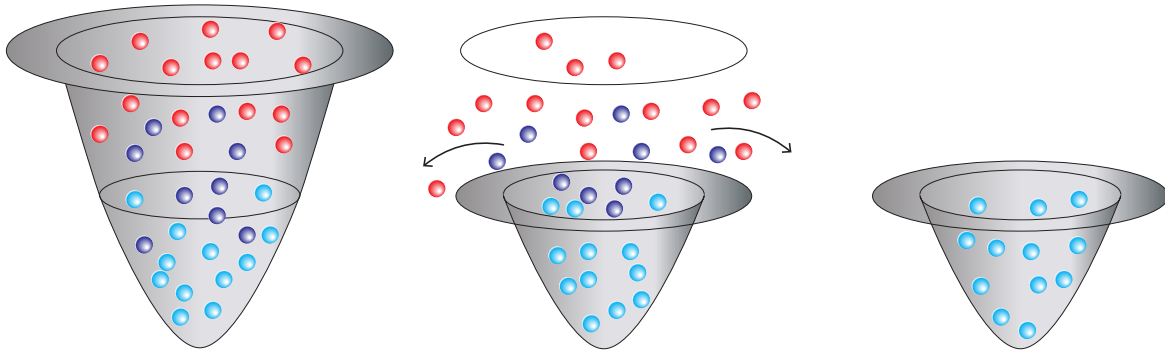

Figure 2.5: Evaporative cooling scheme. A reduction in the beam intensity translates into a decrease of the potential. Thus, the more energetic atoms leave the trap and after some re-thermalization time, the average velocity of the system decreases causing a temperature drop. Figure taken from [36].

2.3.7 Absorption imaging

Once an erbium BEC is obtained, it becomes necessary to have a process which allows to take images of the atomic cloud. This would allow to monitor the cloud behaviour along multiple experimental cycles, this phase is known as Absorption imaging (AI) with its scheme shown in Figure 2.6. To achieve this phase, first we turn off all the lasers and magnetic fields to shoot the atomic ensemble with a resonant light pulse of the near 401 nm transition. As a result, the atoms would absorb the photons and re-emit them in all directions, reducing the intensity in different regions of the laser beam. This shadowed light beam is then received by a CCD camera, which takes an image. To obtain an optical density profile of the cloud, it is required to take two more images. The second one is taken a few ms after the first, and receives the light from a second identical light pulse but once the atomic cloud is gone. Finally, the third one is taken without laser light entering the CCD sensor, and is simply used to quantify any background noise. This three images allow the calculation of a density profile $D(x, y)$ for any pixel located in the image with coordinates x and y by using the Beer-Lambert law [31]

$$D(x, y) = -\ln\left(\frac{I(x, y) - I_D(x, y)}{I_0(x, y) - I_D(x, y)}\right), \tag{2.23}$$

where $I(x, y)$ represents the light intensity measured in the pixel (x, y) for the first image, $I_0(x, y)$ intensity from the second image and $I_D(x, y)$ from the third image. From this density profile, multiple parameters of the cloud can estimated. One of those is the atom number, which can be obtained by integration of $D(x, y)$ and product with the inverted scattering cross-section of erbium. Other parameters are the position and radius of the atomic cloud, which allow relevant calculations such as the cloud temperature. For more information on this process, calculation of parameters or any procedure related with the formation of an erbium BEC refer to [31, 37].
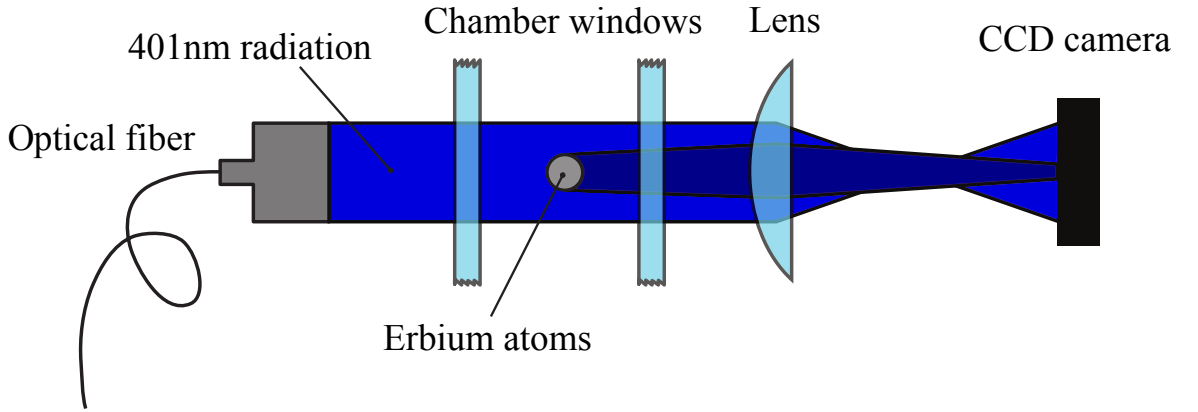

Figure 2.6: Scheme of the absorption imaging process. The atomic ensemble is illuminated with resonant light from the 401 nm transition, and the shadow image is received by the CCD camera. After some few ms, a second picture is taken with an exactly equal light pulse. And finally, a third picture is taken with no light pulse. These three images allow to generate a density image of the atomic cloud. Figure taken from [40]

Diffraction of a Bose-Einstein condensate off a one-dimensional optical lattice potential

In ultracold atoms physics, optical lattices are defined as periodic wave potentials generated by interfering laser beams interacting with an atomic BEC. Its use allows to replicate results from solid state physics, with the interaction between an ultracold atomic ensemble and an optical lattice being equivalent to the role of electrons in an atomic lattice (i.e. a solid-state crystal) [41–43]. However, the use of ultracold systems presents some advantages when comparing with those used in solid state physics. The main one being the capability of changing the optical lattice properties, by simply adjusting parameters like the intensity and detuning of the laser beams forming it. An additional advantage of ultracold atomic systems is the non-existence of crystal defects, which can be a big source of noise in solid states systems [44]. This experiment will seek to study how an erbium BEC behaves when interacting with a one-dimensional optical lattice potential. In this chapter, an introduction describing the theory behind optical lattices will be shown. After this, it follows a brief description of the implemented set up to form the lattice potential by using the erbium transition near 841 nm (see Table 2.2).

3.1 Theoretical description of an optical lattice potential

As it can be seen in Figure 3.1, generating standing wave requires the use of two interfering laser beams, with a detuning δ from the used atomic transition (in this case the near 841 nm erbium transition). The main parameter that allows to characterize the experiment is known as the lattice depth U_0 and will be determined theoretically in this section by assuming some approximations in the atom behaviour. Moreover, the lattice prosperities can be changed by adjusting the optical intensity of the beams as well as the frequency detuning between beams defined here as Δ. To describe theoretically the interaction of an optical lattice with an atomic ensemble, first is important to characterize accurately the interaction with just one of the optical beams forming the lattice.

3.1.1 Dipole interaction of one optical beam

Taken individually, a laser beam would interact with the atomic cloud like a typical optical dipole trap (ODT). Therefore, each beam generates a dipole potential in the atomic ensemble given by Equation

(2.18). However, in this case there is not a far detuning between the laser beams forming the lattice and erbium atomic transitions. Due to this, assuming the optical fields as quasi-electrostatic does not work any more. But, Equation (2.18) holds in any case and can be rewritten when the atoms are approximated as a two level scheme following the behaviour of a classical Lorentz oscillator [13]. For this case, it can be proved that the complex polarizability α has the form:

$$\alpha = 6\pi\epsilon_0 c^3 \frac{\Gamma/\omega_0^2}{\omega_0^2 - \omega^2 - i(\omega^3/\omega_0^2)\Gamma},$$

(3.1)

where ω is the optical frequency of the laser beam interacting with the atom ensemble, ω_0 is the atomic transition and Γ the on-resonance damping rate. Even though this result is obtained when using the classical Lorentz approximation, the same expression can be obtained when considering the semi-classical model of the atom. In which, the atom is considered as a two-level quantum system that interacts with a classical field of light. For the semi-classical model, the damping rate Γ corresponds to the spontaneous decay rate of the excited level and is given by

$$\Gamma_{\text{smcls}} = \frac{\omega_0^3}{3\pi\epsilon_0 \hbar c^3} |\langle e| \mu |g\rangle|^2,$$

(3.2)

where $\langle e| \mu |g\rangle$ stands for the dipole matrix element between ground and excited state. By using Equations (2.18) and (3.1), for the case of large enough detuning δ (making the scattering rate much smaller than Γ) and low enough intensities $I(\vec{r})$ (avoiding saturation of the excited state), the dipole potential $U_{\text{dip}}(\vec{r})$ can be obtained as

$$U_{\text{dip}}(\vec{r}) = -\frac{3\pi c^2}{2\omega_0^3} \left(\frac{\Gamma}{\omega_0 - \omega} + \frac{\Gamma}{\omega_0 + \omega} \right) \cdot I(\vec{r}).$$

(3.3)

Being this equation valid for both the classical and semi-classical model. For most cases, the rotating wave approximation can be applied here because usually the detuning $|\delta| << \omega_0$. Using this approximation, the dipole potential for one laser beam interacting with an neutral atomic ensemble can be obtained as

$$U_{\text{dip}}(\vec{r}) = \frac{3\pi c^2 \Gamma}{2\omega_0^3 \delta} \cdot I(\vec{r}).$$

(3.4)

And by assuming the beam to be a Gaussian beam, Equations (2.19) and (3.4) lead to the exponential behaviour already described in Equation (2.20).

3.1.2 One-dimensional optical lattice potential

After considering only the interaction with just one beam, the optical lattice potential $U_{\text{lat}}(\vec{r})$, generated by two optical beams, has the same relation with the lattice intensity $I_{\text{lat}}(\vec{r})$ than the previous case described in Equation (3.4). Therefore, it can be assumed similarly that

$$U_{\text{lat}}(\vec{r}) = \frac{3\pi c^2 \Gamma}{2\omega_0^3 \delta} \cdot I_{\text{lat}}(\vec{r}),$$

(3.5)

where $I_{\text{lat}}(\vec{r})$ is proportional to the squared absolute value of the summed electric fields $\vec{E}_1(\vec{r}, t)$ and $\vec{E}_2(\vec{r}, t)$ generated by the two beams

$$I_{\text{lat}}(\vec{r}) \propto \left| \vec{E}_1(\vec{r}, t) + \vec{E}_2(\vec{r}, t) \right|^2. \tag{3.6}$$

For the case where both beams are linearly polarized in the arbitrary $\hat{e}_z$ direction, have the same frequency ω and form a perfectly parallel overlay through the x axis, the electric fields have the expression

$$\vec{E}_i(\vec{r}, t) = \hat{e}_z E_{i0}(\vec{r}) \cdot e^{-i(\omega t \pm kx)}, \tag{3.7}$$

with $i \in \{1, 2\}$ and $E_{i0}(\vec{r})$ the electric field amplitude of the laser beam i at the point in space $\vec{r}$ from the beam propagation axis. For beam intensities of the same order $I_1(\vec{r}) \sim I_2(\vec{r})$, the lattice intensity can be approximated as

$$I_{\text{lat}}(\vec{r}) = 4\sqrt{I_1(\vec{r}) I_2(\vec{r})} \cdot \cos^2(kx). \tag{3.8}$$

Therefore, a final expression for the lattice potential can be obtained when combining Equations (3.5) and (3.8). The result is as expected, a temporally static potential with periodicity along the overlaying x axis

$$U_{\text{lat}}(\vec{r}) = U_0(\vec{r}) \cdot \cos^2(kx). \tag{3.9}$$

This important result can be seen in the scheme shown in Figure 3.1. Where, $U_0(\vec{r})$ is known as the lattice depth for which

$$U_0(\vec{r}) = \frac{6\pi c^2 \Gamma}{\omega_0^3 \delta} \cdot \sqrt{I_1(\vec{r}) I_2(\vec{r})}. \tag{3.10}$$

This is a crucial parameter that allows the complete characterization of the optical lattice. In order to estimate it, $I_1(\vec{r})$ and $I_2(\vec{r})$ must be considered as Gaussian beam intensities governed by Equation (2.19). However, for an atomic BEC localized in a given point in space $\vec{r}$, the alignment between optical beams is very sensitive. This means that factors like spacial differences in the propagation axes or different waist sizes between beams, affect very strongly on the effective values of the intensities in Equation (3.10). Due to this, two coordinate systems must be considered to account for the atomic ensemble position relative to the first and second beam. This way, the BEC is located at position $\vec{r}_1$ ($\vec{r}_2$) with respect to beam 1 (beam 2), which has a waist size of w_1 (w_2) at the atomic ensemble position. As a way of illustrating this argument, the expression for a Gaussian beam intensity profile shown in Equation (2.19) will be applied for both beams in Equation (2.19). Using the fact that $I_1(\vec{r})$ and $I_2(\vec{r})$ depend only on the distance with respect to each beam centre, the coordinate system can be changed as $U_0(\vec{r}) = U_0(r_1, r_2)$ with

$$U_0(r_1, r_2) = \frac{12 c^2 \Gamma \sqrt{P_1 P_2}}{\omega_0^3 \delta w_1 w_2} \cdot \exp\left(-\frac{r_1^2}{w_1^2} - \frac{r_2^2}{w_2^2} \right). \tag{3.11}$$

In this expression there are two terms that must be accounted for. The first one corresponds to the fraction, with all terms being experimentally measurable within a reasonable uncertainty value. The second one nonetheless, is formed by two exponentials depending on the beams alignment with respect to the atomic BEC position. Due to this, it is not an easy term to measure because of the big changes that small variation in the position may cause. Therefore, a direct calculation of the lattice depth with the experimental parameters is not feasible and more advanced methods must be considered [45].
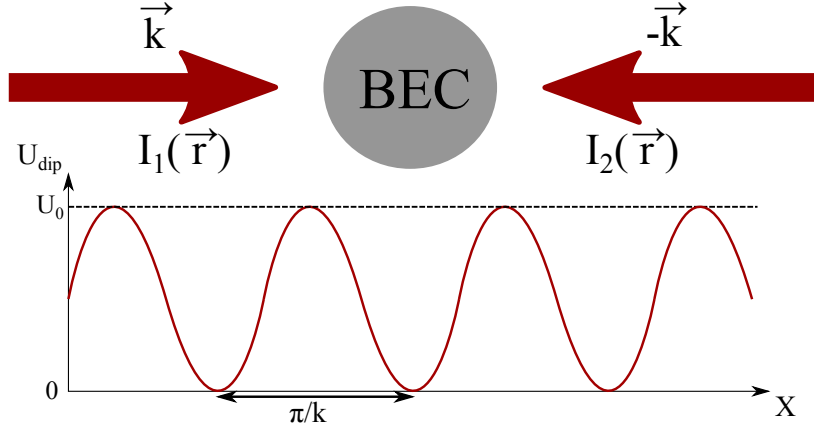
Figure 3.1: Scheme of an atomic BEC interacting with a one dimensional optical lattice potential. For this case, it has been decided that the optical lattice is generated by two counter-propagating laser beams with wave number k, detuned a certain value δ from the erbium near 841 nm transition. Most of the lattice characteristics can be tuned by simply adjusting the beam intensities $I_1(\vec{r})$ and $I_2(\vec{r})$ at the BEC position $\vec{r}$.

Moving optical lattice

Once the lattice potential were obtained for two beams with the same frequency, there is a relevant case of study for which this assumption is not valid. This is the situation in which there is a small detuning Δ between both beams. In this case, an additional temporal phase is added to one of the electric fields in Equation (3.7). This means that the temporally independent expression for the lattice potential of Equation (3.9), becomes temporally dependent with the form

$$U_{\text{lat}}(\vec{r}, t) = U_0(\vec{r}) \cdot \cos^2\left(kx - \frac{\Delta}{2}t\right), \tag{3.12}$$

where the Raman beams intensities have also been assumed to be of the same order $I_1(\vec{r}) \sim I_2(\vec{r})$ at the BEC position $\vec{r}$. This way, the lattice becomes a periodic potential, which moves along the beam propagation axis with time. Allowing for a different interaction process with the atomic ensemble, which will be described in the following section.

3.2 Diffraction of an ultracold atomic ensemble

When an atomic BEC interacts with an optical lattice, there are multiple processes that may be involved. Therefore, different regimes will appear, based on the lattice properties and interaction time with an atomic ensemble. The main ones, which will be discussed in this thesis, are related with diffraction processes of the ensemble. These two are commonly known as the Bragg and Raman-Nath regimes, which will be discussed in this section [46, 47]. To give an idea of how this diffraction effects act over an atomic ensemble, its experimental set-up must be considered analogous to the well-known process of light diffraction. Figure 3.2 shows this analogy between both processes, generating different orders (0th, ±1st ...) as a result. All these orders must fulfil a theoretical restriction known as the Bragg condition, which was initially theorized only for light diffraction by a crystal lattice [48]. However,

this condition is also valid for atomic diffraction, with the detuning Δ between optical lattice beams, acting as the restricted parameter.
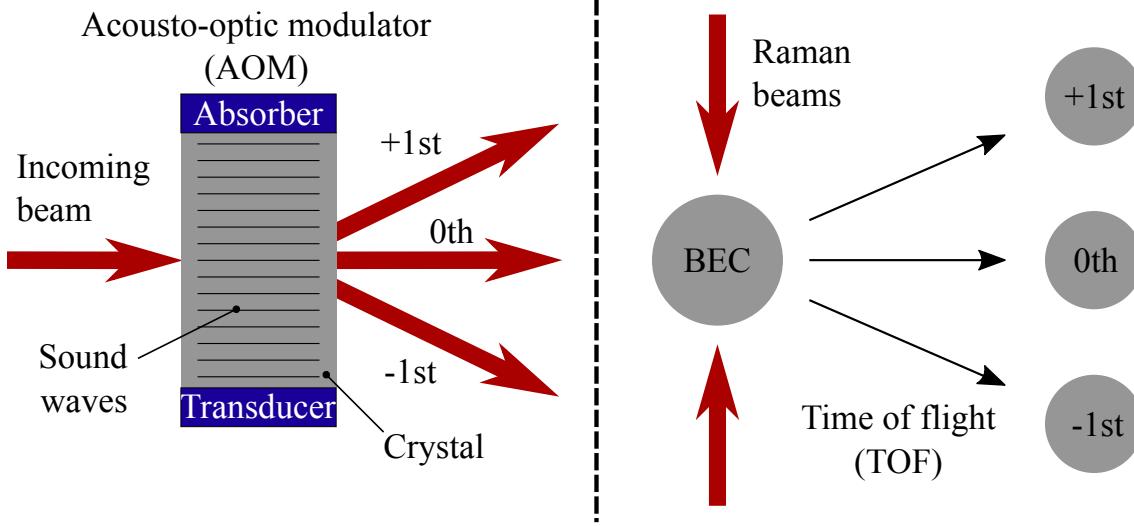

Figure 3.2: Analogy between the processes of light diffraction and atomic diffraction of an ultracold ensemble. The left side shows an light beam being diffracted through the use of an optical device commonly known as an Acousto-optic modulator (AOM). It consists of a solid-state crystal attached to a piezo-electric transducer, which generates sound waves responsible of diffracting the laser beam when it goes through the crystal, acting as an optical medium. On the other hand, the right side shows the diffraction process of an atomic BEC produced by an optical lattice. The ensemble interacts during a certain interaction time t_{int} with the optical lattice. After a waiting time known as Time of flight (TOF), when the ensemble is just falling in vacuum due to gravity, the diffraction process takes place. For both cases, the result generates different orders (0th, ±1st ...), which fulfil the so-called Bragg condition.

3.2.1 Bragg condition

To give an insight on the process leading to diffraction of an atomic ensemble into the N-th order, it is necessary to consider the physical scheme of a $2N$-photon process. Therefore, the diffraction of an ultracold atomic BEC can be viewed as a stimulated Raman transition process [49]. Meaning that one can think of the interaction between light and atoms, as photons from one beam being absorbed by the atomic ensemble while the other beam stimulates the emission of photons. This results in a momentum transfer into the ensemble, which is always "kicked" an invariant momentum quantity in every of this 2-photon interaction. However, in a $2N$-photon process, every on this N-momentum transfers is produced in the optical lattice axis with a 50% chance of being in one direction or the other. This explains the appearance of multiple orders in the diffraction process, they are a result of different $2N$-photon interactions that the atoms inside an ensemble can have. Moreover, it also explains why the separation between orders is the same, it is the displacement produced by the momentum transfer resulting from a 2-photon process after a time of flight (TOF). This momentum transfer is commonly known as the 2-photon recoil $\vec{P}_{\text{rec}}$. To illustrate this, an atom must be considered with mass M and initial momentum $\vec{P}_0 = \hbar \vec{k}_0$ along the lattice x-axis. The atom interacts with two photons, one coming from the left beam with momentum $\hbar \vec{k}_1$ and other from the right beam with $\hbar \vec{k}_2$. Thus, the total initial

momentum of the system before interacting can be expressed as

$$\vec{P}_{\mathrm{i}} = \hbar\vec{k}_0 + \hbar(\vec{k}_1 + \vec{k}_2),\tag{3.13}$$

and the total energy before interaction can also be obtained as

$$E_{\mathrm{i}} = \frac{|\vec{P}_0|^2}{2M} + \hbar(\omega_1 + \omega_2).\tag{3.14}$$

After interacting, the atom absorbs one of the photons and is stimulated by the other. Resulting in the emission of two identical photons in one of the directions. Arbitrarily, the left photon will considered to be absorbed, hence the right one will be stimulated. The total momentum after interaction results

$$\vec{P}_{\mathrm{f}} = \hbar\vec{k}_0 + \hbar(\vec{k}_1 + \vec{k}_2) + 2\hbar\vec{k}_2.\tag{3.15}$$

The total energy can be obtained analogously like

$$E_{\mathrm{f}} = \frac{|\vec{P}_0 + \vec{P}_{\mathrm{rec}}|^2}{2M} + 2\hbar\omega_2,\tag{3.16}$$

where $\vec{P}_{\mathrm{rec}} = \hbar(\vec{k}_1 + \vec{k}_2)$ represents the 2-photon recoil, the momentum transfer to the atom. It is usually reasonable to consider the case in which both beams forming the lattice have approximately the same wave number $|\vec{k}_1| \simeq |\vec{k}_2| \equiv k$. Even though, the beam frequencies differ a given value Δ, this parameter is going to be small enough, allowing for the defined approximation. Due to this, an expression for the 2-photon recoil absolute value can be obtained as

$$|\vec{P}_{\mathrm{rec}}| = 2\hbar k \sin\left(\frac{\theta}{2}\right),\tag{3.17}$$

with θ the angle between wave vectors $\vec{k}_1$ and $\vec{k}_2$, and $k = \frac{2\pi}{\lambda}$ the wave number with wavelength λ.

By using the energy conservation principle with Equations (3.14) and (3.16), the resulting expression gives

$$\Delta_1 = \frac{1}{2M\hbar}\left[|\vec{P}_{\mathrm{rec}}|^2 + 2(\vec{P}_0 \cdot \vec{P}_{\mathrm{rec}})\right].\tag{3.18}$$

This gives the value for which the frequency difference between beams $\Delta = \omega_1 - \omega_2$, fulfils the so-called Bragg condition in a 2-photon process. Therefore when $\Delta = \pm\Delta_1$, the $\pm$1st diffracted order becomes resonant, meaning that the physical system would tend to diffract more atoms into this order. Due to this, one can conclude that the Bragg condition in this experiment restricts Δ and therefore the moving lattice speed, which is governed by Equation (3.12). The situation can be compared with the light diffraction process described in Figure 3.2 for an AOM, with the incidence angle of the incoming beam playing the role of Δ. When this angle fulfils the Bragg condition for the 1st order, it becomes resonant and most of the light will be diffracted through it.

It can be proved that Equation (3.18) generalized for a $2N$-photon has the expression [49]

$$\Delta_n = \frac{1}{2M\hbar}\left[nP_{\mathrm{rec}}^2 + \frac{2(\vec{P}_0 \cdot \vec{P}_{\mathrm{rec}})}{n}\right],\tag{3.19}$$

where $n = \pm 1, \pm 2, ...$ for the different possible diffracted orders. It must be noted that the vectorial product $\vec{P}_0 \cdot \vec{P}_{\text{rec}}$ from Equation (3.19) becomes zero in average for most of the cases. This is due to the fact that an atomic BEC can be considered static with respect to the optical lattice during the interaction time t_{int}. Thus, the resonance condition for the different orders can be obtained from Equations (3.17) and (3.19) as

$$\Delta_n = \frac{2n\hbar k^2}{M},\tag{3.20}$$

for a lattice formed by two counter-propagating waves ($\theta = 0$). From now on, this will be the used expression as a Bragg condition for any n diffracted order.

3.2.2 Rabi oscillations

As it has already been said, the diffraction of an atomic BEC with optical lattices can be considered as a $2N$-photon process. This sort of processes are also known as Raman transitions. The energetic scheme of a 2-photon Raman transition process, like the one discussed in previous section, can be seen in Figure 3.3 [49]. Therefore, the system acts an effective 2-level scheme formed by the initial momentum state $|g, 0\rangle$, together with the final state $|g, 2\hbar k\rangle$ for the 1st diffraction order. This results in Rabi oscillations appearing in the population number of both states, analogously to what happens for the case of a real 2-level system [50]. Thus, the diffraction of an atomic BEC produces oscillations in the population rate of the 1st diffracted order as a function of the interaction time t_{int} between optical lattice and ensemble [51]. In order to make calculations easier, the experimental situation will always use an optical lattice with a squared well in time. This way, the lattice will be on with constant intensity during a time t_{int} and completely off the rest of experimental phases. For the case of a Raman transition like the one disused in Figure 3.3, the population in the first resonant ($\Delta = \Delta_1$) diffracted order $|g, 2\hbar k\rangle$ as a function of the interaction time with the lattice can be expressed as

$$P_1(t_{\text{int}}) = \sin^2\left(\frac{\Omega_{\text{eff}} t_{\text{int}}}{2}\right).\tag{3.21}$$

Resulting in the well-known Rabi oscillations like in the case of an atomic 2-level system. The variable Ω_{eff} is playing here the role of effective Rabi frequency for the 2-photons Raman transition. It is commonly called 2-photon Rabi frequency and, for the first resonant order, it can be expressed as

$$\Omega_{\text{eff}} = \frac{\Omega_1 \cdot \Omega_2}{2\delta}.\tag{3.22}$$

The variables Ω_1 and Ω_2 represent the single photon Rabi frequency for the atomic 2-level system interacting with a photon from the left and right laser beam respectively [50]. By using the electric dipole approximation (the wavelength of the transition can be considered much greater than the typical size of the atom) and considering both beams to be linearly polarized in the z direction, the single photon Rabi frequency can be considered as

$$\Omega_i = \frac{eZ_{12}}{\hbar}|\vec{E}_i(\vec{r})|,\tag{3.23}$$

where e is the electron charge, $eZ_{12} = \langle g| \mu |e\rangle$ the dipole matrix element and $|\vec{E}_i(\vec{r})|$ the electric field amplitude at the point $\vec{r}$ produced by beam $i \in \{1, 2\}$. Therefore, using the relation between electric
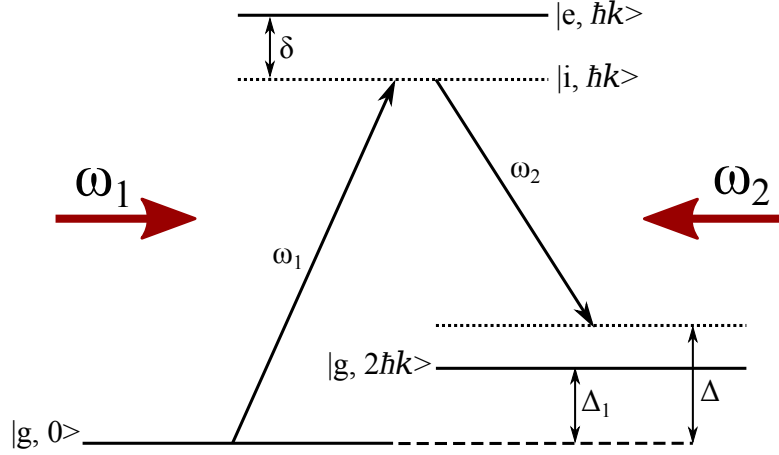
Figure 3.3: Energy scheme of the 2-photon Raman transition process. The 2-level atom is initially in the state $|g, 0\rangle$, with g representing the atomic ground state and 0 the null momentum transferred initially to the atom. Then, the atom absorbs a first photon with frequency ω_1, which stimulates it to an imaginary state $|i, \hbar k\rangle$. Finally, the atom reaches the state $|g, 2\hbar k\rangle$ by emitting a second photon with frequency ω_2 through stimulated emission. It must be noted that the momentum transfer has been considered for two counter-propagating photons ($\theta = \pi$ in Equation (3.17)), and also that Δ_1 represents the resonance condition for the first order given by Equation (3.20) with $n = 1$. Therefore, when $\Delta = \Delta_1$ the condition is fulfilled for this order and the energetic transition gets enhanced. Moreover, to avoid real excitation of the atom into $|e, \hbar k\rangle$, which produces spontaneous emission processes, the detuning from atomic resonance δ must be large enough with $\delta \gg \Delta$.

field amplitude and optical intensity in vacuum is given by

$$|\vec{E}_i(\vec{r})| = \sqrt{\frac{2}{c\epsilon_0}} \sqrt{I_i(\vec{r})}. \tag{3.24}$$

A final relation between the 2-photon Rabi frequency and the optical lattice depth can be obtained simply by using the two previous expressions together with Equations (3.10) and (3.22) as [47]

$$U_0 = 2\hbar\Omega_{\text{eff}}, \tag{3.25}$$

where the semi-classical approximation has been used $\Gamma = \Gamma_{\text{smcl}}$ given by Equation (3.2). This shows a direct relation between the 2-photons Rabi frequency of the diffraction process and the optical lattice depth. It had been shown that this is an important factor required to characterize the system but it could not be estimated experimentally in an accurate way. Now, it is possible to estimate the optical lattice depth by obtaining just the 2-photon Rabi frequency. It must be noted that the linear factor $2\hbar$ may not hold for some cases, where a really high accuracy must be needed, so multiple alternative calibration methods have been proposed [47, 52–54]. However, the topic is out of reach for this thesis, with a complex calibration of the lattice being a possible pending job for the future. As a side note, the calculations shown here can be generalized for $2N$-photon processes [55]. With the effective Rabi frequency for any resonant n diffracted order being

$$\Omega_{\text{eff}}^{(n)} = \frac{(\Omega_1 \cdot \Omega_2)^n}{2^{4n-3}((n-1)!)^2 \delta^n \omega_r^{n-1}}. \tag{3.26}$$

Here, the commonly used parameter ω_r is known as recoil frequency and has the expression

$$\omega_r = \frac{\Delta_1}{4} = \frac{\hbar k^2}{2M}. \tag{3.27}$$

Note that Equation (3.22) can be reached for the first order $n = 1$ with Equation (3.26).

3.2.3 Diffraction regimes

Once the interaction process between an optical lattice and atomic BEC has been described, one can take a closer look to the system in a more general approach. This way, two different regimes can be distinguished by analysing the Hamiltonian for atoms interacting with an optical lattice as [46]

$$\hat{H} = \frac{\hat{p}^2}{2M} + U_{\text{lat}}, \tag{3.28}$$

where U_{lat} represents the lattice potential described by Equation (3.9). Therefore, the resulting Schrödinger equation looks like

$$i\hbar\dot{\psi}(x,t) = \underbrace{-\frac{\hbar^2}{2M}\frac{\partial^2\psi(x,t)}{\partial x^2}}_{\text{Kinetic term}} + \underbrace{2\hbar\Omega_{\text{eff}}\cos^2(kx)\cdot\psi(x,t)}_{\text{Lattice potential term}}, \tag{3.29}$$

with $\psi(x,t)$ being the wave function of the 2-level atoms and $\dot{\psi}(x,t) \equiv \frac{\partial\psi(x,t)}{\partial t}$ the temporal partial derivative. In order to reach this expression, it is required to assume that the atomic detuning is much greater than the excited state linewidth $\delta \gg \Gamma, \Omega_{\text{eff}}, \omega_r$. This avoids the excitation of most of the atoms into its excited state, allowing for $\psi(x,t)$ to be considered the wave function of atoms in the ground state. Moreover, the system has been assumed to be a one dimensional problem, with the atoms being only able to interact with the optical lattice in the x direction. As it can be seen, the rest of parameters related with atomic, optical and alignment properties of the system are conveniently hidden within the 2-photon Rabi frequency Ω_{eff}. For the case in which Ω_{eff} is not time dependent, Equation (3.29) enters under the classification group known as Mathieu's differential equations [56]. This type of equation can not generally be solved analytically, which results in the need of simplifying the problem by distinguishing different regimes. This thesis will approach the topic by discussing only the two main regimes in a qualitative way. For a more in-depth study, please refer to [45–47, 57, 58].

Raman-Nath regime

In the case of very short interaction times t_{int}, the atoms move only by a very small distance compared to the lattice period π/k. Therefore, the movement of atoms during the lattice pulse can be neglected, which allows to remove the kinetic energy term in Equation (3.29) (first term on the right hand side). This is known as Raman-Nath approximation and was first introduced in the study of light diffraction with sound waves, acting as a thin grating [59]. After removing the kinetic energy term, the Schrödinger equation becomes solvable. This solution splits the ground state wave function into multiple n terms with a momentum transfer of $2n\hbar k$, representing the diffraction orders described

during this section.

$$\psi(x,t) = \sum_{n=-\infty}^{+\infty} g_n(t)e^{i2nkx}, \tag{3.30}$$

with the coefficients of every diffraction order given by Bessel functions of the first kind [46]

$$g_n(t) = (-i)^n J_n(\Omega_{\text{eff}}t). \tag{3.31}$$

Therefore, the resulting population probability of any diffraction order n after an interaction time with the lattice of t_{int} can be expressed as

$$P_n(t_{\text{int}}) = J_n^2(\Omega_{\text{eff}}t_{\text{int}}). \tag{3.32}$$

As a result, multiple diffraction orders are generated in this regime, each one with a population probability given by Equation (3.32). From a physical point of view, the diffraction into multiple orders can be understood as a result of the energy uncertainty due to short interaction times. Initially, this number of diffraction orders increases with t_{int}. However, after a certain limit, the number of orders stops increasing by effect of the kinetic energy term in the Hamiltonian. This can be justified by using the argument of energy-momentum conservation. Because the dispersion relation is quadratic for atoms and linear for light, which avoids the conservation of energy and momentum for higher orders. This effect can again be compared with the process of phase mismatch that appears in non-linear optics. The saturation of diffraction orders is what restricts the regime, and it can be proved, that the Raman-Nath approximation holds only for interaction times $t_{\text{int}} \ll 1/\sqrt{2\Omega_{\text{eff}}\omega_r}$ [57].

Bragg regime

For the case of longer interaction times, the effects of energy-momentum conservation are very strong and do not permit the kinetic energy term removal in the Schrödinger equation. This kinetic contribution increasingly limits the number of allowed diffraction orders, at the point of permitting only two for a low enough value of the lattice depth. Because in very long interaction times, the energy uncertainty stops being a contributing factor. Moreover, the kinetic term dominates, forcing the Bragg condition with the argument of energy-momentum conservation. Due to this, the described case is commonly known as the Bragg scattering regime, because of its similarities with Bragg diffraction of light through a thick grating in optics, as already discussed in this section. It means that, in order to diffract the atomic ensemble into a given n order, the Bragg condition given by Equation (3.20) must be fulfilled. This way, the whole system can be understood as a $2N$-photon Raman process behaving like an effective 2-level system. Resulting in Rabi oscillations appearing between the n and 0th order for varying interaction times. This means that for the Bragg regime, all the theoretical processes described in Sections 3.2.1 and 3.2.2 have a physical correspondence with the system behaviour.

3.3 Experimental realization of a one-dimensional optical lattice

The optical lattice, required to achieve the diffraction processes of an ultracold atomic ensemble, is obtained with the use of two counter-propagating optical beams. The experimental set-up used can be seen in Figure 3.4. The laser beams used to for the lattice are generated by a titanium-sapphire laser, which is frequency stabilized by a wave-meter allowing to use the erbium transition near 841 nm (see

Table 2.2). In order to have a great control over the interaction time with the atom ensemble, both laser beams are coupled into AOMs. This way, only the first orders of the AOMs are coupled into the fibres R1 and R2, allowing to switch the optical lattice at very fast times on the order of a few hundred nanoseconds [60]. The polarization of both beams is being controlled with the use of $\lambda/2$ wave-plates together with polarizing beam spliters (PBSs). This allows to set the linear polarization axis of both beams in the same axis z, which has been a required condition in Sections 3.1.2 and 3.2.2.
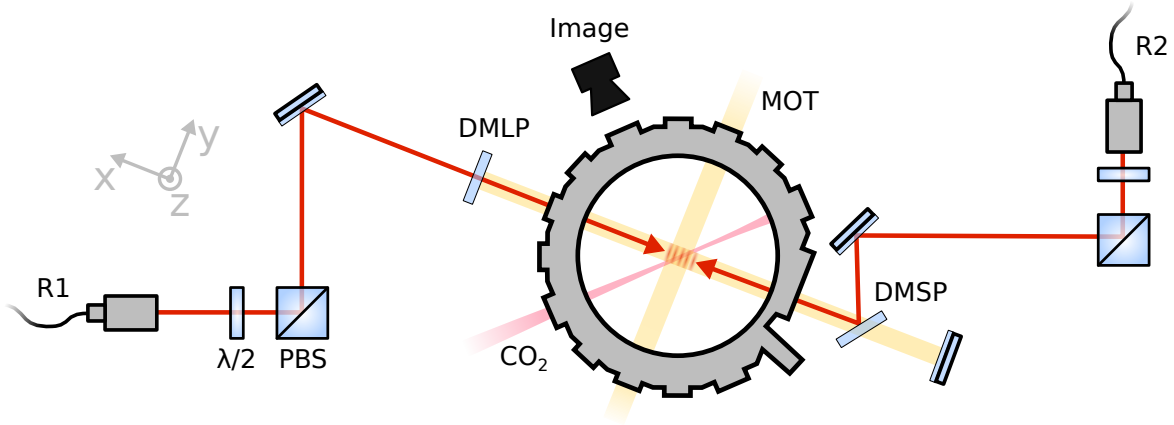
Figure 3.4: Experimental set-up for the optical lattice beam formed inside the UHV main chamber. The laser beams forming this lattice were detuned a value δ from the used erbium transition of 841 nm, and are represented by the two counter-propagating red arrows. These beams have been coupled inside the chamber through one of the MOT axis, by using dicrotic long-pass (DMLP) and short-pass (DMSP) mirrors. Figure taken from [60].

Towards Raman manipulation of spin-momentum state components

After the theoretical description of the Raman processes occurring in the diffraction of ultracold atomic ensembles, the following step consists in the manipulation of momentum and spin states components. The process has a strong resemblance with the previously described, with the added factor that now every momentum state also carries a different internal energy state. This is due to Raman transitions taking place inside the Zeeman levels that erbium's ground state was split into. For the experimental process to function as expected, it is required a given magnetic field $\vec{B}_R = B_R \vec{e}_x$ along the optical beams axis x. This field will produce the Zeeman splitting of the ground state, and the Raman beams will be in charge of producing the transitions, separating the atomic ensemble into multiple energy levels. However, the two photon detuning condition must be fulfilled for this process to happen, and now it corresponds with the energy difference between two Zeeman split states $\Delta E_R = g_J \mu_B B_R$ [50]. Due to this, knowing the exact value of ΔE_R becomes a key factor, and any background magnetic fields affecting the BEC can produce non-desired mixed transitions in the energetic scheme. For this reason, a preparatory experiment must be carried out, that allows the estimation of ΔE_R and helps with the compensation of background fields in favour of the known $\vec{B}_R$ field.

4.1 Radio frequency transitions and the Stern-Gerlach experiment

The objective of this experiment is to quantify the Zeeman splitting induced into an erbium BEC. As it can be seen in Figure 2.1, the energetic ground state of erbium has a total electronic angular momentum of $J = 6$. When the atomic ensemble is being affect by a magnetic field $\vec{B}_H$, the ground state gets Zeeman split into $2J + 1 = 13$ energy states with the secondary quantum number m_J = -6, -5, ..., +6, each state with energy

$$E_{Ze} = g_J \mu_B m_J B_H, \tag{4.1}$$

where g_J represents the Landé g-factor and for this case it is $g_J \approx 1.166$ [50]. Due to the way in which the experimental set-up is constructed, the MOT's 583 nm beam light that interacts with erbium in the z axis, by pushing the atoms against gravity, is σ^- polarized [31]. Due to the fact that this beam interacts mostly with the atomic ensemble, it pumps the atoms into the energetic state with $m_J = -6$. Therefore, the atomic ensemble becomes spin polarized. To allow for transitions between

these different Zeeman states, the atomic ensemble must interact with a radio frequency (RF) pulse. Moreover, in order to distinguish which spin states the RF-pulse has transitioned the atomic ensemble into, a Stern-Gerlach experiment must be performed. This consists in the use of an inhomogeneous magnetic field $B_{\mathrm{IH}}(\vec{r})$ that separates the atomic BEC spatially according the quantum number m_J. The force that allows this is commonly called Stern-Gerlach force and is due to the non-zero gradient applied to the Zeeman term in the hamiltonian [50]

$$\vec{F}_{\mathrm{SG}}(\vec{r}) = \mathbf{\nabla}(\vec{\mu} \cdot \vec{B}_{\mathrm{IH}}(\vec{r})), \tag{4.2}$$

where $\vec{\mu}$ represents the atomic magnetic moment. Therefore, for $B_{\mathrm{IH}}(\vec{r})$ pointing in any arbitrary z direction, the force applied to the different $2J + 1$ levels can be obtained as

$$\vec{F}_{\mathrm{SG}}(\vec{r}) = -g_J \mu_B m_J \frac{\partial B_{\mathrm{IH}}(\vec{r})}{\partial z}, \tag{4.3}$$

which is m_J dependant and produces, as a result, different contributions to the energetic states. This force will make possible the separation of a BEC in Zeeman orders after a given TOF. The use of RF-transitions together with this SG-force permits the creation of an experimental set-up that can quantify the energetic difference between neighbouring Zeeman orders

$$\Delta E_{\mathrm{Ze}} = g_J \mu_B B_{\mathrm{H}}. \tag{4.4}$$

For a given spatially homogeneous field $\vec{B}_{\mathrm{H}}$, interacting initially with an atomic ensemble. The experimental procedure can be described as follows:

- 2 ms after the evaporation phase end, the RF-pulse is applied while $\vec{B}_{\mathrm{H}}$ is kept unchanged. This RF-pulse has a given duration t_{RF}, an intensity I_{RF} and a frequency ν_{RF}. As a result, the erbium BEC transitions between the initial state $m_J = -6$ to $m_J = -5, ..., +6$, only if $\nu_{\mathrm{RF}} \approx \frac{\Delta E_{\mathrm{Ze}}}{\hbar}$ the resonant frequency for the Zeeman transition. Moreover, due to the fact that these transitions also result in Rabi oscillations, the magnitudes t_{RF} and I_{RF} must be adjusted to produce $\frac{\pi}{2}$ pulses and favour the population transference into the rest of Zeeman states.

- After the BEC interaction with the RF-pulse, the ensemble falls due to gravity during a time of flight t_{TOF}. In this time period, the magnetic field gradient $B_{\mathrm{IH}}(\vec{r})$ is activated and the atomic BEC receives a state dependant Stern-Gerlach force given by Equation (4.3). This results in the spacial separation of the Zeeman levels after the TOF, which can be imaged by the absorption imaging phase.

As a result, the experiment allows to measure the resulting orders after a RF-BEC interaction. By varying ν_{RF}, one can make a measurement of the resonant frequency to the Zeeman splitting produced by any homogeneous field $\vec{B}_{\mathrm{H}}$. In addition to the transition's line-width estimation, which is a parameter deeply related to the stability of $\vec{B}_{\mathrm{H}}$ during the interaction time t_{RF}. To conclude, the experiment allows to measure the Zeeman splitting of any given field $\vec{B}_{\mathrm{H}}$ and compensate for the effect that produces by adjusting the offset coils inside the vacuum chamber. This adjust the field to a value that reduces to the minimum $\Delta E_{\mathrm{Ze}} \approx 0$. After this, a known field in the desired Raman beams x direction can be added to the system. By repeating now the same RF measurement, one obtains a fairly good estimation of the Zeeman splitting produced by the known field in the x direction ΔE_{R}. This

value will give the two photon detuning condition for Raman manipulation in the following section. For a broader description of the procedure and experimental set-up refer to [31].

4.2 Raman manipulation of spin-momentum state components

Once the previous experiment has allowed to characterize the magnetic field $\vec{B}_R$ along the quantization axis x, Raman transitions between the Zeeman split states generated by $\vec{B}_R$ can be obtained with the use of two counter-propagating beams. As can be seen in Figure 4.1, the optical set-up is very similar to the previous case. The two main differences are the addition of a magnetic field $\vec{B}_R$ along the Raman beams x axis, and the change from linear to circular $\sigma^{\pm}$ polarization in the optical beams. As a result, now the $2N$-photon Raman transitions generate orders that not only have different momentum components but also different spin values, in this case m_J = -6, -4, -2, 0, +2, +4, +6.
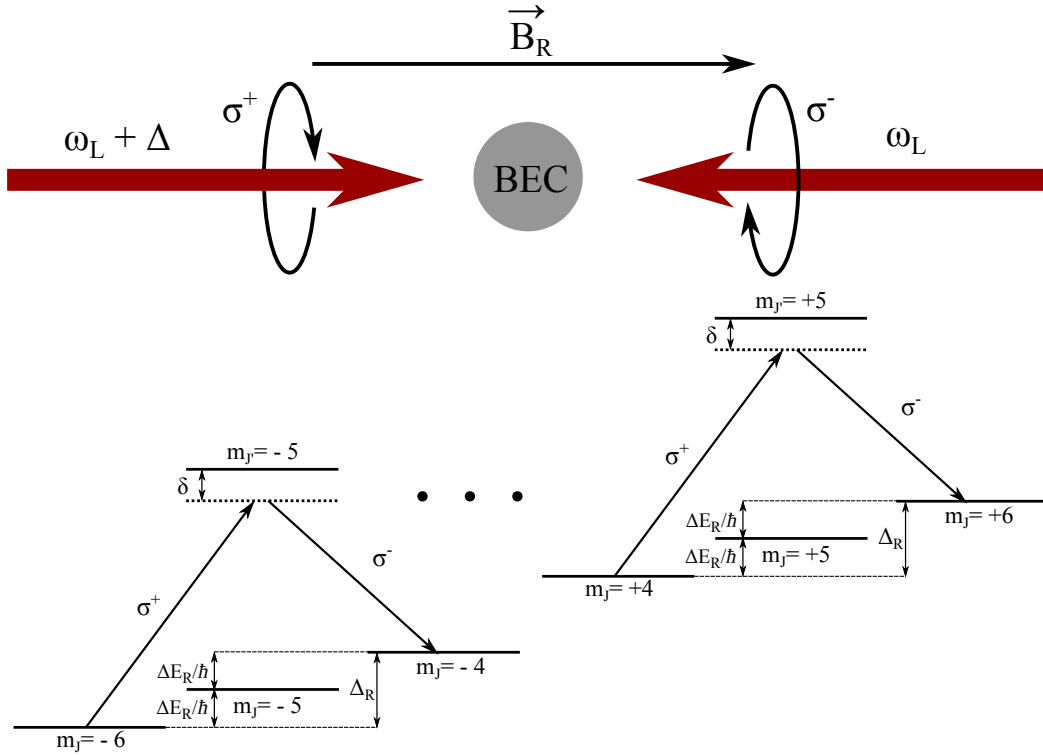
Figure 4.1: Experimental and energetic scheme of the $2N$-photon Raman transition process in the spin-momentum configuration. In this case, the optical scheme is very similar to the described in Chapter 3 with the addition of a magnetic field $\vec{B}_R$ in the beams direction x and the circular polarization $\sigma^{\pm}$ of both Raman beams. Moreover, the energetic scheme also relates to the Raman process described in Figure 3.3, with the only difference that now the two photon detuning condition becomes the so-called Raman condition given by $\Delta_R \equiv 2\Delta E_R/\hbar$. As a result, the orders generated in the Raman process not only have different momentum components but also spin values m_J = -6, -4, -2, 0, +2, +4, +6, which means internal energetic differences in the generated orders.

This optical set-up, with both beams and magnetic field along the same direction, requires the use of circular polarized light in both beams to make the transitions between Zeeman states possible. Due to this, the 2-photon Raman process can not transfer the atoms between two contiguous Zeeman states

like $m_J = -6 \rightarrow m_J = -5$ [50]. This has been avoided with other optical set-ups where a circularly polarized beam in the quantization axis (magnetic field direction) together with a transversal linearly polarized beam were used [61]. However, this limitation is not that important for this case because in erbium $J = 6$, which generates as already announced 7 different orders m_J = -6, -4, -2, 0, +2, +4, +6. Therefore for transitions with $\Delta m_J = 2$, the Raman condition for the two-photon detuning Δ becomes

$$\Delta_R = 2 \cdot \frac{\Delta E_R}{\hbar},\tag{4.5}$$

where ΔE_R represents the energy difference of contiguous Zeeman states, which is proportional to the field in the quantization axis $\vec{B}_R$ as shown in Equation 4.4. Lastly, it must be noted that due to the large magnetic moment of erbium, a slight misalignment of the field with the Raman axis can produce mixed transitions in the energetic scheme. This is why, the RF measurement is required to adjust the field and make sure it is aligned as much as possible with the Raman axis.

Results and discussion

Once the theoretical description of the experiment has been completely introduced, the following part consist in the exposition of the obtained results together with a discussion concerning its correspondence with the announced theory. Due to this, the first step must be the Raman beams characterization with the measurement of each beam radius. This will allow in the next parts to make a direct correlation between beam power and intensity, which will be crucial for the whole experimental characterization.

5.1 Measurement of the Raman beams radius

These laser beams of the 841 nm transition have been considered during all the theory as Gaussian beams. Therefore, they are described spatially by Equation (2.19), which gives the relation between beam power P and maximum intensity I_0 as

$$I_0 = \frac{2P}{\pi w_0^2},\tag{5.1}$$

where w_0 represents the beam radius at the atomic cloud position. Thus, a measurement of this quantity must be performed in order to obtain I_0 from the beam power. Figure 5.1 shows both horizontal and vertical measurements for the two beams with the use of a knife-edge method. These data points were fit to an error function, which gave the estimations for w_0 in every case. From averaging the vertical and horizontal estimations of w_0 one gets the final measurement to be

$$w_{01} = (0.4961 \pm 0.0012)\text{mm} \qquad\qquad w_{02} = (0.8778 \pm 0.0024)\text{mm}.$$

Note that the use of 1 and 2 for the Raman beams is also used as a distinction tool in Figure 3.4. As one can observe, the difference in beam size is approximately a factor of 3 between both beams. This must be compensated by adjusting the beam powers; however, it is a strong mismatch in the parameters that could not be solved due to time constraints. Therefore, the discussion part of the following measurements will have into account this mismatch in beam sizes as a source of possible non-correspondence between theory and experiment.

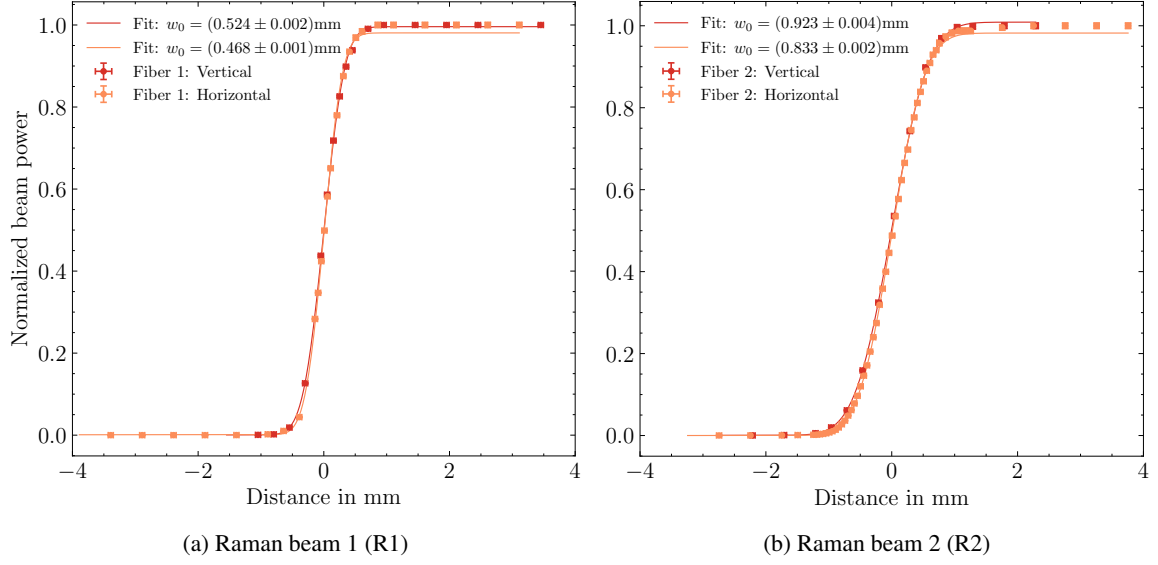(a) Raman beam 1 (R1)

(b) Raman beam 2 (R2)

Figure 5.1: Beam radius measurement of the Raman beams performed with a knife-edge method. The beam profile was measured at approximately the atomic cloud position. Each of the beams were measured in a vertical (red) and horizontal (orange) position.

5.2 Characterization of the 841 nm erbium transition with a BEC

The following part consists in studying the 841 nm erbium transition by blocking arbitrarily the beam R2 and allowing R1 to interact freely with the erbium BEC. This way, the Raman beam frequency can be locked in every cycle to a specific value. After an interaction time of 10ms in the final part of the evaporation phase, the atomic ensemble falls freely during a TOF of 20ms. Then, the measurement is taken with the absorption imaging phase. From these measurements, the number of atoms can be estimated and the result, after scanning the frequency of R1, is shown in Figure 5.2. The data with a maximum of $N_{\mathrm{max}} = 34849$ atoms was taken as normalization factor. As it can be seen from the image, the plot shows a drop in the atom number when R1 is locked to a wavelength of approximately 840.98827 nm in air. This is because most of the atoms forming a BEC are resonant at this wavelength and get excited by the R1 beam, which expel them out of the ensemble and reduce drastically the atom number. In order to avoid effects like power broadening, the optical power of R1 has been kept as low as possible: $P_{\mathrm{R1}} = (49.0 \pm 0.5)\mathrm{mW}$. This way, the Gaussian fit performed in Figure 5.2 gives an estimation of the resonant wavelength λ_0^* and the linewidth broadened mostly due to the beam power $\Delta\nu_{\mathrm{PB}}$ as

$$\lambda_0^* = 840.988266(2)\mathrm{nm} \qquad\qquad \Delta\nu_{\mathrm{PB}} = (3600 \pm 1700)\mathrm{kHz}$$

The result is a quite accurate estimation of λ_0^* while the calculation for $\Delta\nu_{\mathrm{PB}}$ is not. The main reason is due to limitations in the scanning precision of the wave-meter, which was locking the laser. In any case, the measurement of $\Delta\nu_{\mathrm{PB}}$ is helpful when comparing it to the theoretical linewidth of the transition $\Delta\nu_0 = \Gamma/2\pi = 7.96\,\mathrm{kHz}$ (see Table 2.2). Giving a real scenario of how big the one-photon detuning δ must be to make reasonable the approximations used for the Raman transition processes. On the other hand, the estimation of λ_0^* contains a source of errors that has not been considered so far.
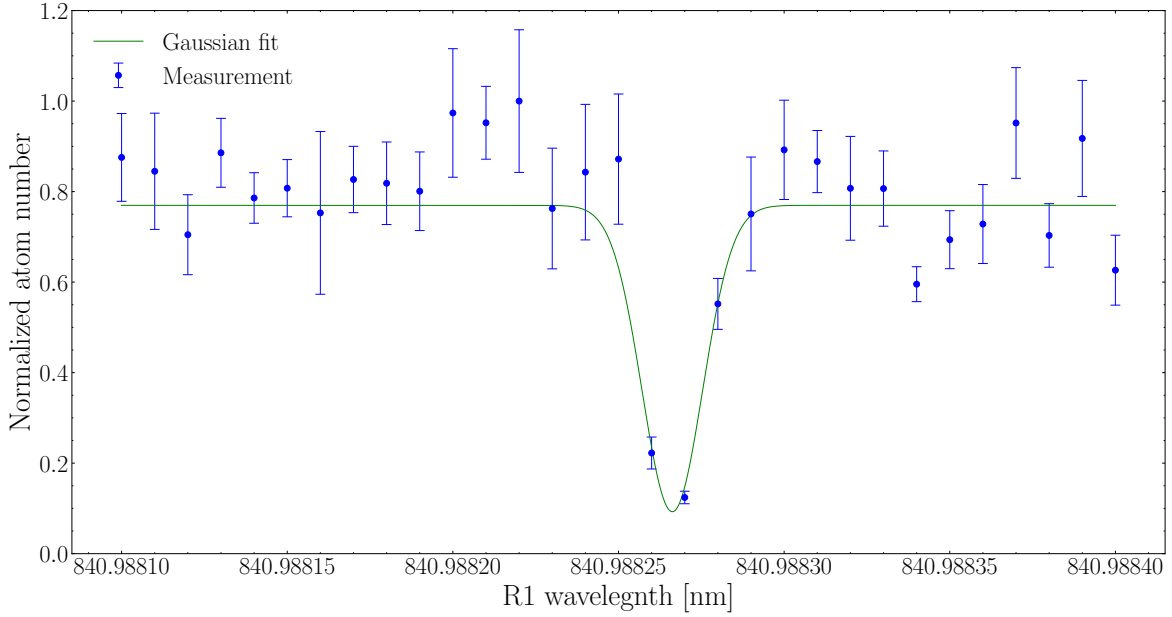
Figure 5.2: Interaction of an erbium BEC with the beam R1. The plot shows the atom number of the BEC, normalized to the maximum measured value, as a function of the R1 wavelength in air. The interaction between R1 and the atomic ensemble lasts 10ms before the end of evaporation phase in every experimental cycle. Each measured point has been obtained by averaging the atom number of 5 experimental cycles.

This is the uncertainty coming from the laser frequency lock, which can not be assumed to remain constant and may shift during measurements. For this reason, the one-photon detuning δ estimation will be obtained with by using as resonance wavelength in air the following value:

$$\lambda_0 = 840.98827(1)\text{nm}$$

5.3 Diffraction of an erbium BEC with a 1D-lattice

Now, it is the moment to study the diffraction of an erbium BEC with the described Raman lattice set-up. In order to do this, the one photon detuning δ must be measured. Due to the conclusions made in previous section, the optical frequency of the Raman beams has been chosen for this whole part to be $\lambda_R = 840.98880(1)\text{nm}$. Thus, the resulting value for δ turns out to be

$$\delta = 2\pi c \cdot \left(\frac{1}{\lambda_0} - \frac{1}{\lambda_R} \right) = 2\pi \cdot (225 \pm 6)\text{MHz} \approx 1.8 \times 10^{-5} \cdot \Delta\nu_0.$$

Therefore, the approximations used for the Hamiltonian in Section 3.2.3 are fulfilled. Because $\delta \gg \Gamma, \Delta\nu_0$ being the decay rate Γ and natural linewidth $\Delta\nu_0$ of the 841 nm transition (see Table 2.2). Another approximation that has been performed along this thesis results to be $\delta \gg \omega_r = \frac{\Delta_1}{4}$, with the 2-photon recoil frequency Δ_1 given by Equation (3.20) with $n = 1$. From this expression one can get

the value of Δ_1 to be

$$\Delta_1 = \frac{2\hbar k^2}{M} = 2\pi \cdot (6.713 \pm 0.004)\text{kHz}.$$

This result proves the approximation $\delta \gg \Delta_1$ to also be reasonable within the described situation. Therefore, the different theoretical regimes seem to be valid and a more in-depth study is possible.

5.3.1 Bragg regime

As seen in Chapter 3, the Bragg regime is achieved only for long interaction times and when the Bragg condition is being fulfilled. To achieve it, the detuning between Raman beams has been set to Δ_1. The result is an effective two level system between the 0th and +1st diffraction orders acting as ground and excited states respectively. This generates Rabi oscillations for different interaction times t_{int} with frequency Ω_{eff} between the ground and excited state population rates, with the last one ideally governed by Equation 3.21. This effect has been observed for the case of optical power in the Raman beams chosen like: $P_1 = (3.05 \pm 0.05)\text{mW}$ and $P_2 = (9.10 \pm 0.05)\text{mW}$. These powers allow to estimate the "effective" intensity of the lattice as

$$I_{\text{eff}} = \sqrt{I_1 \cdot I_2} = (7.7 \pm 0.4)\text{kW m}^{-2}.$$

Figure 5.3 shows the effect of Rabi oscillations between the 0th and 1st orders for the exposed value of I_{eff}. These images are just a small sample of all the measured for this same situation but different values of t_{int}. From each image, the population rate of any i order with $i \in \{0, 1\}$ can be estimated as

$$P_i = \frac{N_i}{N_0 + N_1}, \tag{5.2}$$

where N_0 and N_1 are the number of atoms in each diffraction order. Therefore, it is possible to measure the population rate in each picture and plot it as a function of t_{int}. This is shown in Figure 5.4.

(a) $t_{\text{int}} = 60\mu s$ (b) $t_{\text{int}} = 120\mu s$ (c) $t_{\text{int}} = 240\mu s$
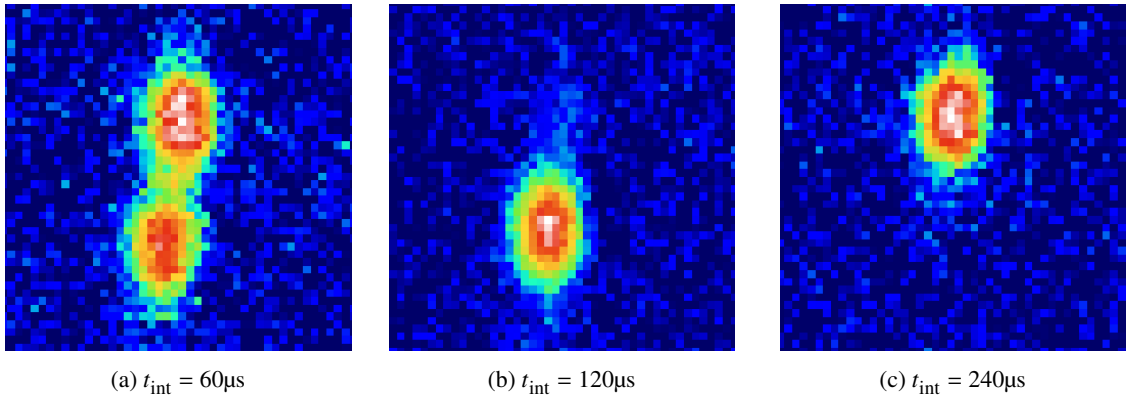
Figure 5.3: Diffracted ultracold erbium ensemble after an interaction time with the lattice t_{int} and a TOF= 19ms. One can observe the effect of Rabi oscillations due to different t_{int} values. The top atomic cloud corresponds to the 0th diffraction order while the bottom cloud is the 1st. Each image has been normalized with respect to the maximum and minimum value in the frame. The used camera is rotated 90° counter-clockwise, resulting in the separation of orders in the vertical axis of the frames. The effective intensity of the lattice used was $I_{\text{eff}} = (7.7 \pm 0.4)\text{kW m}^{-2}$.
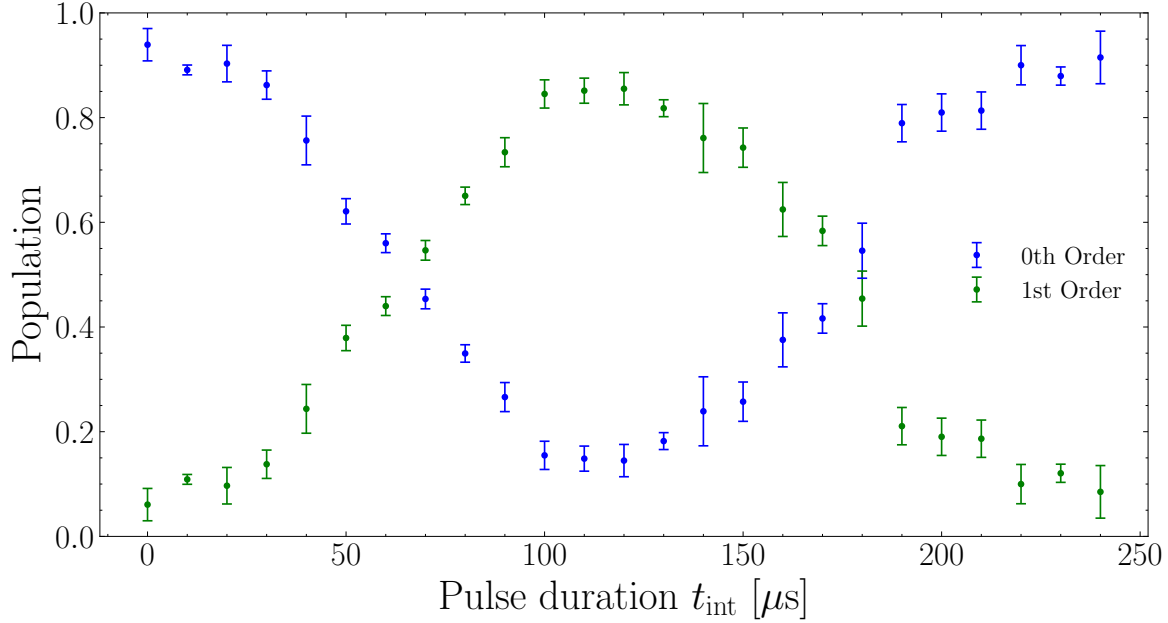
Figure 5.4: Population rate as a function of the interaction time between erbium BEC and Raman lattice. The plot shows Rabi oscillations in rate populations of the 0th and 1st diffraction orders. Each pair of points has been taken by averaging 5 different images. The Raman lattice had an effective intensity of $I_{\text{eff}} = (7.7 \pm 0.4)\text{kW m}^{-2}$.

The plot confirms the theory and shows Rabi oscillations in an effective 2-level system as a predominant effect for this regime of parameters. Once this set of data is obtained, one can perform a more in-depth analysis of the oscillations. As it has been said, Equation 3.21 must be fulfilled in this regime for the behaviour of population in the 1st diffracted order P_1. This way, a sine squared function fit can be performed to this population rate. However, in order to account for factors like noise or coherent losses in the BEC, a damped term has been added. Thus, the fitted function expression results

$$f_{\text{fit}}(t_{\text{int}}) = A\exp(-bt_{\text{int}}) \cdot \sin^2\left(\frac{\Omega_{\text{eff}}t_{\text{int}}}{2} + \phi\right) + y_0, \tag{5.3}$$

where A, b, Ω_{eff}, ϕ and y_0 are free parameters of the fit. This allows the estimation of relevant system parameters such as the 2-photon Rabi frequency for any value of I_{eff}. The result can be seen in Figure 5.5 for three different values of I_{eff}. From this analysis, one can easily see a proportional relation between I_{eff} and Ω_{eff}, which is also described in the theory. When combining Equations (3.25) and (3.11) one gets

$$\Omega_{\text{eff}} = \left(\frac{3\pi c^2 \Gamma}{\omega_0^3 \delta \hbar}\exp\left(-\frac{r_1^2}{w_1^2} - \frac{r_2^2}{w_2^2}\right)\right) \cdot I_{\text{eff}}, \tag{5.4}$$

which contains an exponential term describing how "good" the Raman beams are aligned with respect to the erbium BEC. Unfortunately, this term can not be measured independently within a reasonable value of uncertainty. However, it can be estimated with the obtained data by simply performing a linear fit to the measured values of Ω_{eff} as a function of I_{eff}. This can be seen in Figure 5.6.
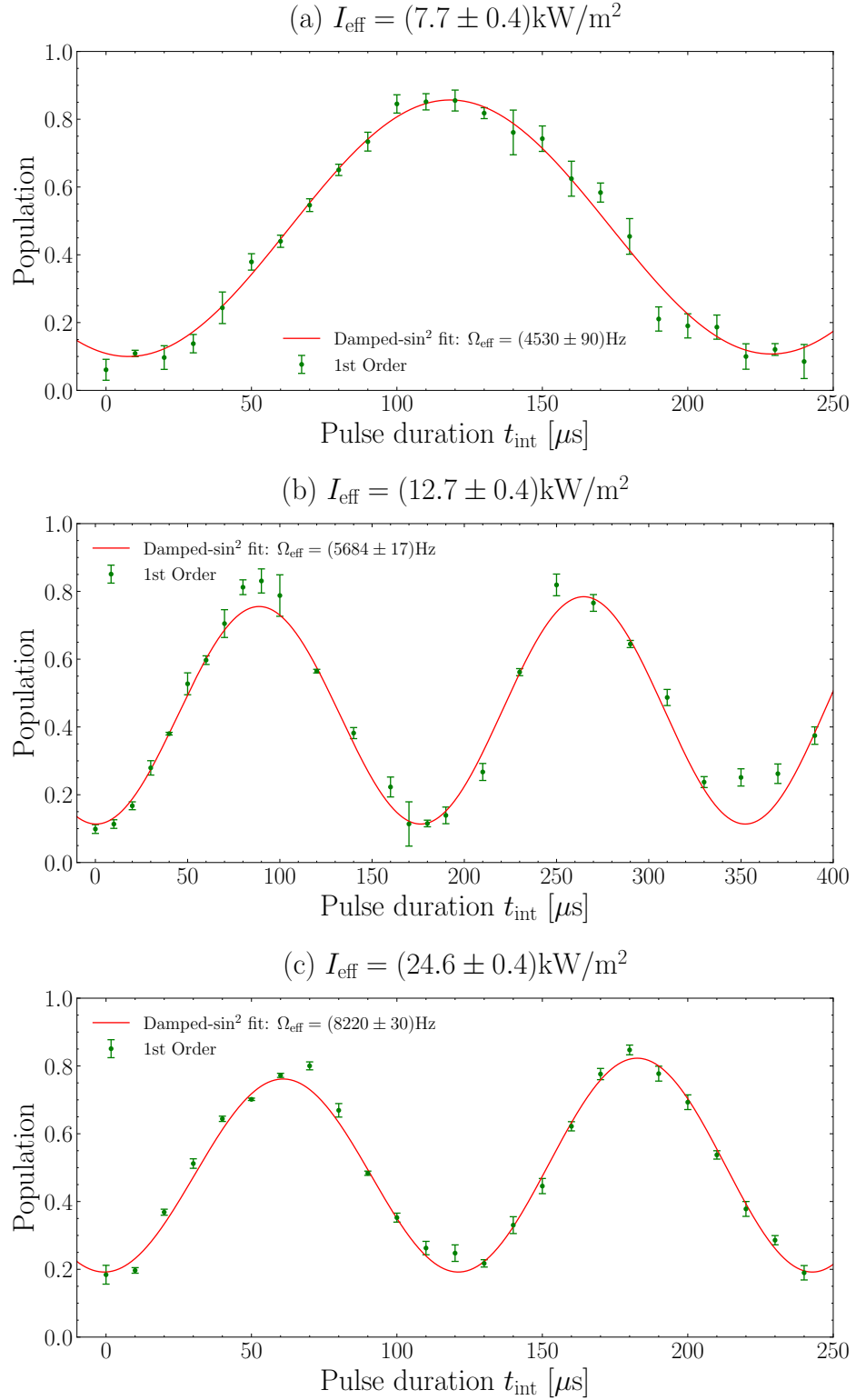
Figure 5.5: Fit of a damped sine squared function to the population rate for different values of I_{eff}. The objective is to characterize the Rabi oscillations in this state and obtain an estimation of the 2-photon Rabi frequency Ω_{eff}.
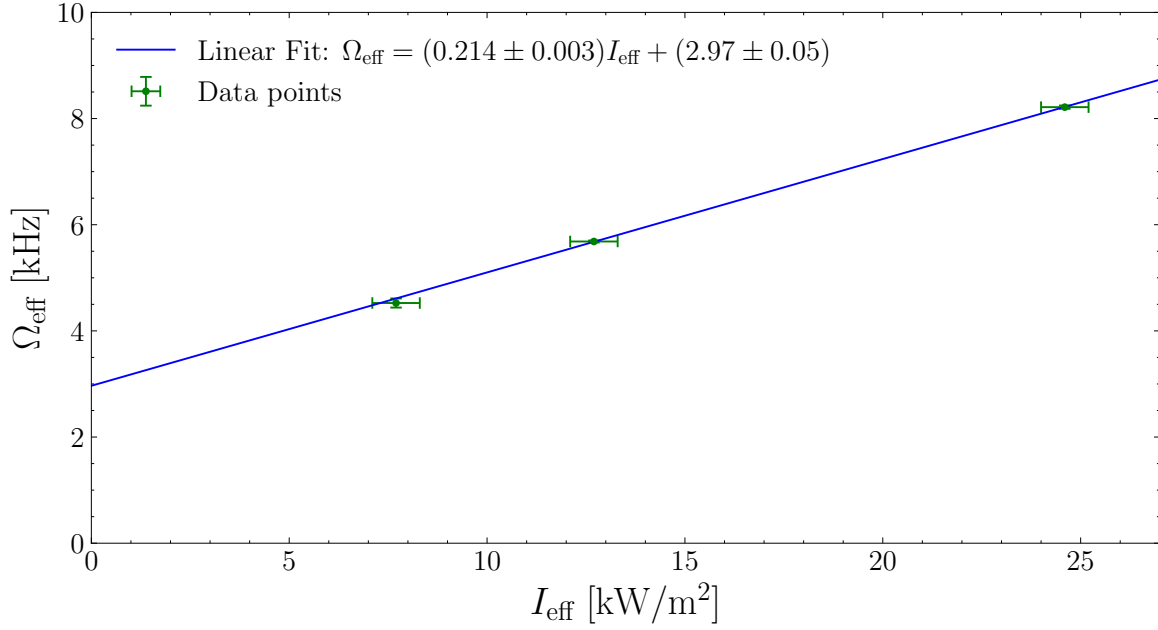
Figure 5.6: Linear fit of the 2-photon Rabi frequency as a function of the effective intensity in the lattice.

As a result, the linear fit seems to fulfil very accurately the measured data behaviour, which also coincides with theory. One could argue, the amount of data points to not be high enough. This is due to time constrains at the moment of taking the data, as different experimental problems appeared together with the requirement of measuring more data that will be shown below. In any case, the linear fit also shows a discrepancy with Equation (5.4), which consist in a non-zero intercept of (2.97 ± 0.05)kHz. This can be due to different reasons, the main one being the differences between Raman beam sizes. It could be a mayor factor because together with the beam misalignment, there will be a major difference between the optical intensities perceived by the BEC. This produces a shift in the lattice potential, which in principle should not affect these measurements for small shift values, but in the case of very big ones it could be a responsible factor. Other possibility is that the little amount of points covers a non-linear behaviour for small values of I_{eff} for unknown reasons. In any case, the slope estimation of (0.214 ± 0.003)kHz m^2 kW^{-1} allows the calculation of a "misalignment" factor as

$$\beta \equiv \exp\left(-\frac{r_1^2}{w_1^2} - \frac{r_2^2}{w_2^2}\right) = (8.5 \pm 0.3) \cdot 10^{-3},$$

which gives a maximum misalignment distance between the BEC position and R1/R2 beams' centre to be $r_1^{\text{max}} = (1.083 \pm 0.003)$mm and $r_2^{\text{max}} = (1.384 \pm 0.006)$mm respectively. These values are within a reasonable order, but the alignment factor seems to be of very low quality for the implemented theoretical model.

5.3.2 Raman-Nath regime

Once, the Bragg regime has been characterized, it is the moment of briefly showing that the Raman-Nath regime is also achievable in this experimental set-up. After ramping up the effective intensity in the optical lattice to $I_{\text{eff}} = (42.12 \pm 0.5)\text{kW m}^{-2}$, and setting the 2-photon detuning between R1 and R2 to zero. The result can be seen in Figures 5.7 and 5.7, where an average of over 104 different pictures has been performed. As it can be seen, up to 5 different diffraction orders can be distinguished, which confirms the described theory and shows the experimental set-up capability to achieve the Raman-Nath regime.
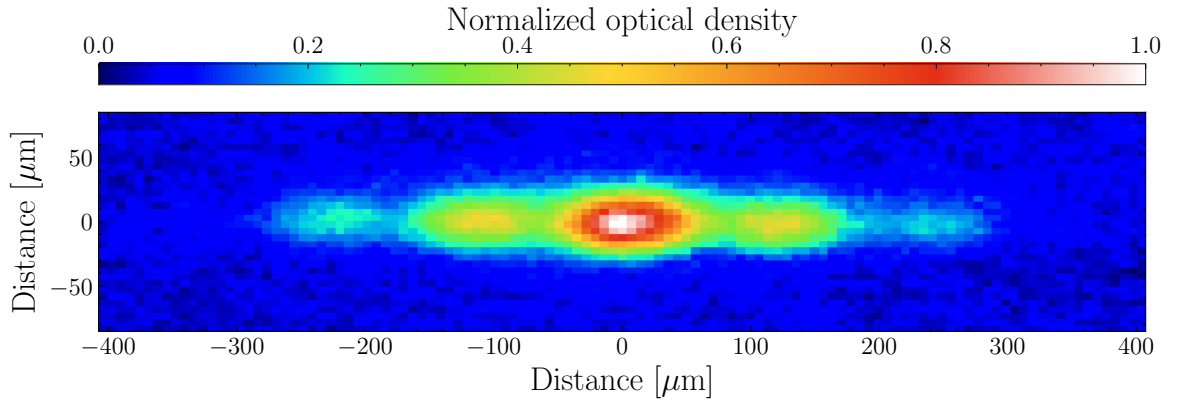
Figure 5.7: Absorption image of a multiple orders diffracted BEC after a TOF of 19 ms. The result was obtained after an average of over 104 different pictures with an effective intensity of $I_{\text{eff}} = (42.12 \pm 0.5)\text{kW m}^{-2}$. The image has been rotated to match the gravitational axis with the up-down axis in the frame.
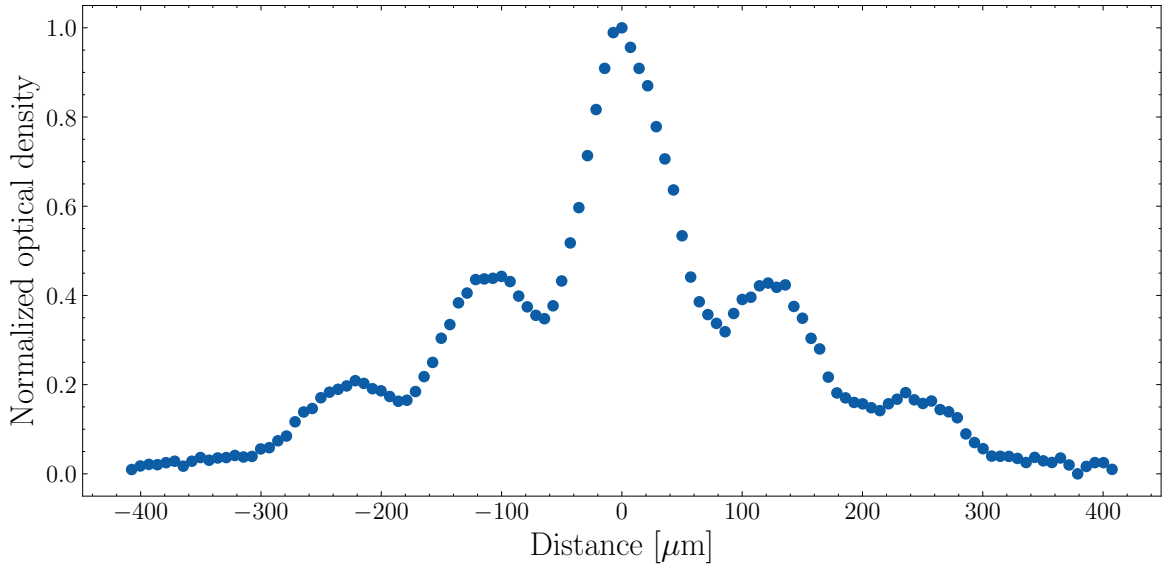
Figure 5.8: Average cut performed to the image shown in Figure 5.7

5.4 Magnetic fields characterization with RF transitions

After characterising an optical set-up that results in Raman transitions between components in the momentum space, the following goal is already described in Chapter 4. This objective consists in obtaining Raman transitions between components in the spin and momentum space. But first, it is required the use of RF transitions to estimate the Zeeman splitting caused by the magnetic fields inside the vacuum chamber. This way, the effect can be compensated first and then an extra field can be added along the quantization axis of the Raman beams, which will be required for the Raman transitions. Section 4.1 describes this in further detail, while here the focus will be in analysing the measured data. Figure 5.9 shows two reference samples of the measurements. An erbium BEC interacts with an RF-pulse during 0.4 ms and falls through a gradient field of approximately 4 G/cm during the TOF of 19 ms, which allows the separation between Zeeman states due to the Stern-Gerlach force. When the RF-pulse frequency is far away from the Zeeman resonance $\omega_{Ze} \equiv \Delta E_{Ze}/\hbar$ given by Equation 4.4, the result is shown in Figure 5.9(a). The RF transitions are being suppressed and the BEC remains mostly in the state $m_J = -6$ due to the experimental set-up configuration (see Section 4.1). On the other hand, when the RF-pulse frequency is close to ω_{Ze}, the transitions into other Zeeman levels are allowed, as shown in Figure 5.9(b). Therefore, by scanning the RF-pulse frequency in the region of Zeeman resonance and comparing the population in different states, one can get an estimation of ω_{Ze} produced by any homogeneous magnetic field $\vec{B}_H$. Thus, the measurements of ω_{Ze} for three different homogeneous fields can be seen in Figure 5.10.

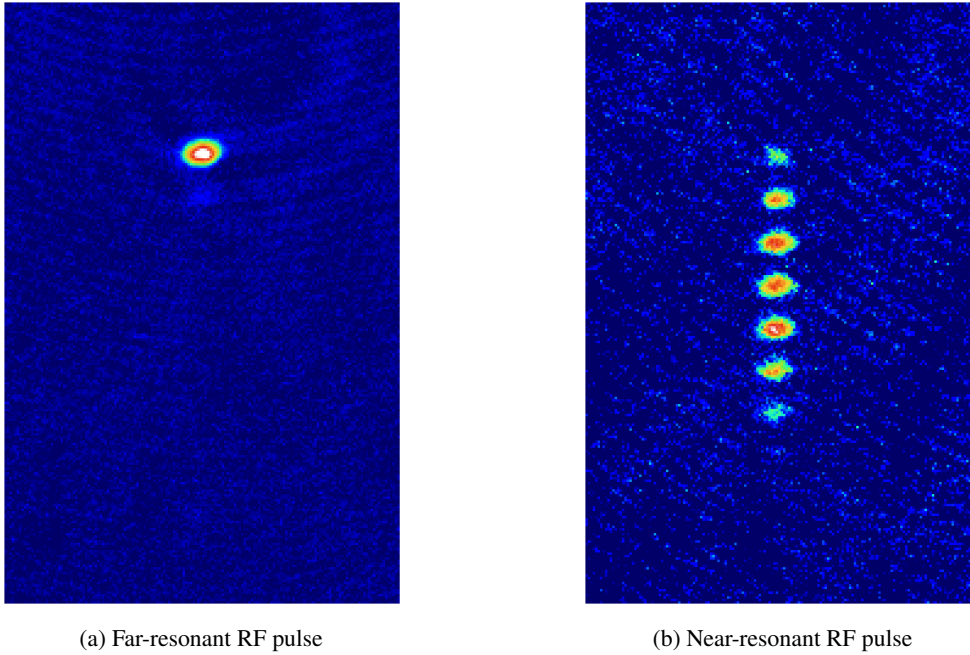(a) Far-resonant RF pulse   (b) Near-resonant RF pulse

Figure 5.9: Comparative set of two different interactions between an erbium BEC and a RF-pulse. Both images were taken after an interaction time with the RF-pulse of 0.4 ms and a TOF of 19 ms. During this time of flight a gradient field of approximately 4 G/cm was applied in order to separate the different m_J orders. The gradient field direction was being applied along the gravitational axis, which corresponds to the vertical direction in both images.
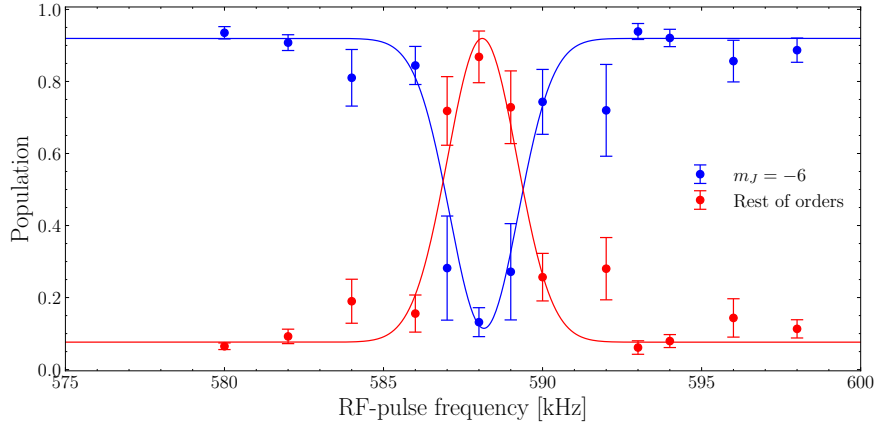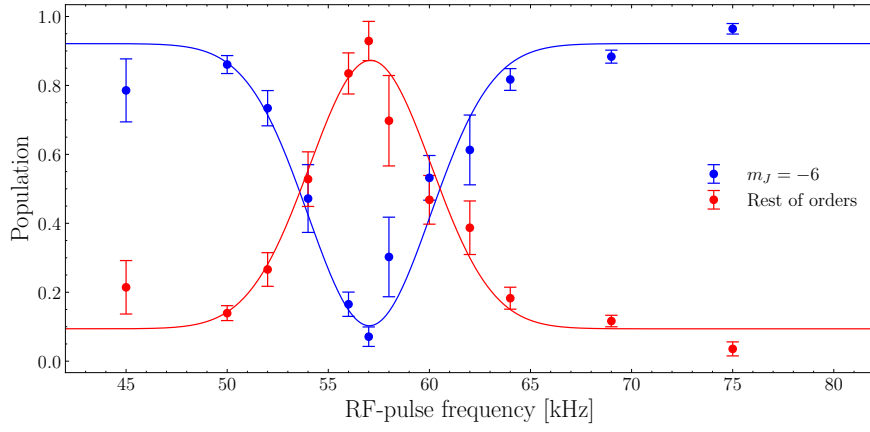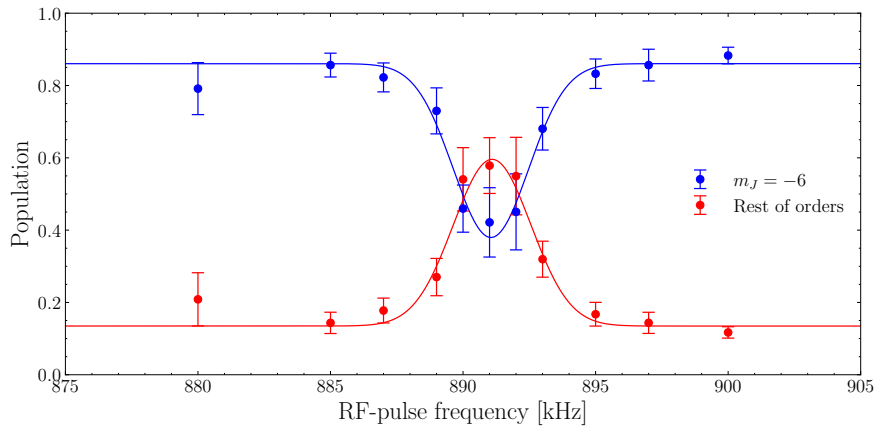
(a) Experiment magnetic field $\vec{B}_\mathrm{H}$

(b) Compensated magnetic field $\vec{B}_\mathrm{Comp}$

(c) Added magnetic field $\vec{B}'_\mathrm{H} = \vec{B}_\mathrm{Comp} + B_\mathrm{R}\vec{e}_x$

Figure 5.10: Measured frequency spectrum of the RF transitions for different homogeneous magnetic fields causing the splitting of Zeeman states in the erbium BEC. This data has been obtained measuring the population in each state and comparing the result for state $m_J = -6$ with the added population of the rest m_J =-5, -4, ..., +6. A Gaussian fit has been applied in each set of data in order to obtain an estimation of the resonant frequencies and transition linewidths.

Each plotted data in the three parts of Figure 5.10 corresponds to a ratio of the atom number in the ground state $m_J = -6$ and the rest of states m_J =-5, -4, ..., +6. The different fields are: $\vec{B}_H$ the default magnetic field affecting the BEC during the experiment, $\vec{B}_{Comp}$ the compensated field with offset coils in order to make ω_{Ze} as low as possible, and $\vec{B}'_H = \vec{B}_{Comp} + B_R \vec{e}_x$ the result of adding to the compensated field and extra one in the Raman beams direction for the following section. By applying a Gaussian fit to each set of data, an estimation of relevant parameters like the Zeeman resonant frequencies ω_{Ze} and the RF transition linewidths $\Delta\omega_{Ze}$ were obtained:

Magnetic field	ω_{Ze} [kHz]	$\Delta\omega_{Ze}$ [kHz]
$\vec{B}_H$	588.1 ± 0.1	1.1 ± 0.4
$\vec{B}_{Comp}$	57.06 ± 0.15	3.0 ± 0.9
$\vec{B}'_H$	891.08 ± 0.14	1.4 ± 0.7

Table 5.1: Estimation of the Zeeman resonant frequencies ω_{Ze} and the RF transition linewidths $\Delta\omega_{Ze}$ from the Gaussian fits performed in Figure 5.10.

These results are reasonable and for the case of $\Delta\omega_{Ze}$ show how stable are the Zeeman splitting and magnetic field. As a result, one can conclude for the next section that the Raman condition for the 2-photon detuning Δ must be of approximately $2 \cdot 890$ kHz with an error margin of 58 kHz given by ω_{Ze} for the compensated field $\vec{B}_{Comp}$.

5.5 Raman transitions in the spin-momentum space

Finally, the last measurement achieved in this thesis correspond to Raman transitions between Zeeman states. In order to achieve it, the offset coils of the experiment have been configured to produce the magnetic field $\vec{B}'_H$, which is mostly pointing throughout the Raman beams axis. After this, the Raman beams were re-aligned and their radius at the BEC position reduced to:

$$w_{01} = (134 \pm 2)\mu m \qquad\qquad w_{02} = (142 \pm 2)\mu m.$$

Moreover, the beams polarization was changed from linear to circular, in order to achieve the experimental set-up described in Section 4.2. The optical powers for each beam were approximately 50mW. And, the 2-photon detuning between beams was adjusted by using the value obtained at the previous section and Equation (4.5) as $\Delta_R \approx 2 \cdot 890$ kHz. There result was the obtention of Raman transitions in the spin-momentum space, which can be seen in Figure 5.11. For both cases, the images were taken after an interaction time of $220\,\mu s$ with the Raman beams and a TOF of $20\,ms$. The only difference between both images is that Figure 5.11(a) had no gradient field being applied during the TOF and 5.11(b) did have it of roughly 4G cm^{-1}. The result is that the orders generated in the first image do not experience an Stern-Gerlach force, described by Equation 4.3, while the orders in the second image are affected from this effect. Due to this, the Raman orders are separated in the gradient direction as a function of their spin value m_J, apart from the separation due to different momentum transfer that remains unaltered. This effect proves without a doubt the internal energetic difference between orders and the achievement of Raman transitions in states with different spin. After this achievement, an in-depth study of the experimental system will remain for a future work.

(a) Without magnetic gradient
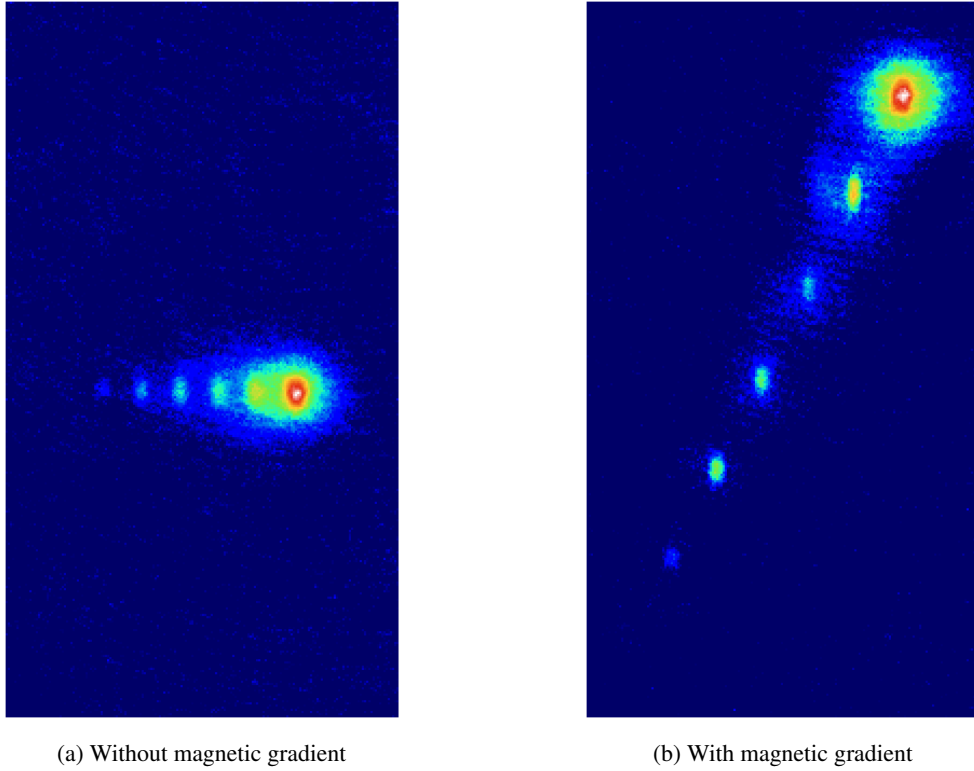
(b) With magnetic gradient

Figure 5.11: Comparative picture of Raman transitions between spin-momentum orders with and without gradient field interaction. This gravitational direction is again matched with the gradient field and corresponds to the left-right axis on both frames. In (b), the Stern-Gerlach force separates the diffracted orders as a function of the spin value m_J throughout the gradient field direction. Proving the internal energy difference in each order.

Conclusion and outlook

In the present master thesis, several effects related to the energetic manipulation of an ultracold ensemble of erbium atoms were studied. The main part is related to the study of optical manipulation with the use of a lattice potential generated by two counter-propagating light beams. These laser beams were detuned with respect to a narrow line erbium transition near 401 nm, which generates 2-photon Raman transitions into different energetic states. Initially the process was used only for transitions between the momentum space for the same internal state of erbium. Leading to the study of the Bragg and Raman-Nath regimes that allowed to characterize the experimental set-up and the interaction process between erbium and light.

The following part consists in the use of Raman transitions along the spin-momentum space, which is generated by Zeeman splitting taking place in the ground state of erbium. In order to achieve it, the magnetic fields of the experiment have been characterized and adjusted with the use of radio frequency transitions and a Stern-Gerlach force. This way the 2-photon detuning condition between Raman beams can be estimated, leading to the achievement of 2-photon transitions between Zeeman and momentum states.

The implemented experimental set-up is the ground work for the generation of synthetic magnetic fields in ultracold erbium clouds. A process that could unravel some limitations of neutral atomic systems, by generating an artificial Lorentzian force like in charged particles. Possibly leading to a quantum Hall regime that could enable studies of topological quantum computation [15].

Bibliography

[1] S. N. Bose, "Plancks gesetz und lichtquantenhypothese", Zeitschrift für Physik **26**, 178–181 (1924).

[2] A. Einstein, "Quantentheorie des einatomigen idealen gases", Sitzungsberichte der Preussischen Akademie der Wissenschaften **22**, 261–267 (1924).

[3] A. Einstein, "Quantentheorie des einatomigen idealen gases. zweite abhandlung", Sitzungsberichte der Preussischen Akademie der Wissenschaften **50**, 3–10 (1925).

[4] K. B. Davis et al., "Bose-einstein condensation in a gas of sodium atoms", Phys. Rev. Lett. **75**, 3969–3973 (1995).

[5] M. H. Anderson, J. R. Ensher, M. R. Matthews, C. E. Wieman and E. A. Cornell, "Observation of bose-einstein condensation in a dilute atomic vapor", Science **269**, 198–201 (1995).

[6] C. C. Bradley, C. A. Sackett, J. J. Tollett and R. G. Hulet, "Evidence of bose-einstein condensation in an atomic gas with attractive interactions", Phys. Rev. Lett. **75**, 1687–1690 (1995).

[7] S. Stellmer, M. K. Tey, B. Huang, R. Grimm and F. Schreck, "Bose-einstein condensation of strontium", Phys. Rev. Lett. **103**, 200401 (2009).

[8] Y. Takasu et al., "Spin-singlet bose-einstein condensation of two-electron atoms", Phys. Rev. Lett. **91**, 040404 (2003).

[9] M. Lu, N. Q. Burdick, S. H. Youn and B. L. Lev, "Strongly dipolar bose-einstein condensate of dysprosium", Phys. Rev. Lett. **107**, 190401 (2011).

[10] K. Aikawa et al., "Bose-einstein condensation of erbium", Phys. Rev. Lett. **108**, 210401 (2012).

[11] J. Klaers, J. Schmitt, F. Vewinger and M. Weitz, "Bose–einstein condensation of photons in an optical microcavity", Nature **468**, 545–548 (2010).

[12] S. Baier et al., "Realization of a strongly interacting fermi gas of dipolar atoms", Phys. Rev. Lett. **121**, 093602 (2018).

[13] R. Grimm, M. Weidemüller and Y. B. Ovchinnikov, "Optical dipole traps for neutral atoms", Advances In Atomic, Molecular, and Optical Physics **42**, edited by B. Bederson and H. Walther, 95–170 (2000).

[14] X. Cui, B. Lian, T.-L. Ho, B. L. Lev and H. Zhai, "Synthetic gauge field with highly magnetic lanthanide atoms", Phys. Rev. A **88**, 011601 (2013).

[15] Y.-J. Lin, R. L. Compton, K. Jiménez-García, J. V. Porto and I. B. Spielman, "Synthetic magnetic fields for ultracold neutral atoms", Nature **462**, 628–632 (2009).

[16] C. Mosander, "Xxx. on the new metals, lanthanium and didymium, which are associated with cerium; and on erbium and terbium, new metals associated with yttria", The London, Edinburgh, and Dublin Philosophical Magazine and Journal of Science **23**, 241–254 (1843).

[17] W. Klemm and H. Bommer, "Zur kenntnis der metalle der seltenen erden", Zeitschrift für anorganische und allgemeine Chemie **231**, 138–171 (1937).

[18] J. Emsley, *The elements (oxford chemistry guides)*, 3rd ed. (Clarendon Press; Oxford University Press, Oxford; New York, 1998).

[19] A. Frisch, "Dipolar quantum gases of erbium", PhD thesis (July 2014).

[20] H. Y. Ban, M. Jacka, J. L. Hanssen, J. Reader and J. J. McClelland, "Laser cooling transitions in atomic erbium", Opt. Express **13**, 3185–3195 (2005).

[21] J. E. Sansonetti and W. C. Martin, "Handbook of basic atomic spectroscopic data", Journal of Physical and Chemical Reference Data **34**, 1559–2259 (2005).

[22] J. J. McClelland, "Natural linewidth of the 401−nm laser-cooling transition in Er I", Phys. Rev. A **73**, 064502 (2006).

[23] J. E. Lawler, J.-F. Wyart and E. A. D. Hartog, "Atomic transition probabilities of er i", Journal of Physics B: Atomic, Molecular and Optical Physics **43**, 235001 (2010).

[24] E. A. D. Hartog, J. P. Chisholm and J. E. Lawler, "Radiative lifetimes of neutral erbium", Journal of Physics B: Atomic, Molecular and Optical Physics **43**, 155004 (2010).

[25] R. J. Lipert and S. C. Lee, "Isotope shifts and hyperfine structure of erbium, dysprosium, and gadolinium by atomic-beam diode-laser spectroscopy", Applied Physics B **57**, 373–379 (1993).

[26] A. Kramida, Y. Ralchenko and J. Reader, *Nist atomic spectra database (version 5.8)*, (2020) https://physics.nist.gov/asd.

[27] W. Pauli, "Über den zusammenhang des abschlusses der elektronengruppen im atom mit der komplexstruktur der spektren", Zeitschrift für Physik **31**, 765–783 (1925).

[28] M. Ueda, *Fundamentals and new frontiers of bose-einstein condensation* (WORLD SCIENTIFIC, 2010).

[29] C. J. Pethick and H. Smith, *Bose–einstein condensation in dilute gases*, 2nd ed. (Cambridge University Press, 2008).

[30] L. de Broglie, "The reinterpretation of wave mechanics", Foundations of Physics **1**, 5–15 (1970).

[31] J. Ulitzsch, "Erzeugung eines bose-einstein-kondensats aus erbiumatomen in einer quasi-elektrostatischen dipolfalle", PhD thesis (Rheinischen Friedrich-Wilhelms-Universität Bonn, Dec. 2016).

[32] T. Hänsch and A. Schawlow, "Cooling of gases by laser radiation", Optics Communications **13**, 68–69 (1975).

[33] H. J. Metcalf and P. van der Straten, *Laser cooling and trapping*, 1st ed. (Springer, New York, 1999).

[34] J. Dalibard and C. Cohen-Tannoudji,
      "Laser cooling below the doppler limit by polarization gradients: simple theoretical models",
      J. Opt. Soc. Am. B **6**, 2023–2045 (1989).

[35] P. Zeeman, "The effect of magnetisation on the nature of light emitted by a substance",
      Nature **55**, 347–347 (1897).

[36] M. Rehberger,
      "Ultracold erbium atoms in far-detuned optical traps - construction of a zeeman-slower",
      MA thesis (Rheinische Friedrich-Wilhelms-Universität Bonn, Bonn, Germany, 2013).

[37] R. V. Röll, "Ultracold erbium atoms in a quasi-electrostatic optical dipole trap",
      MA thesis (Rheinische Friedrich-Wilhelms-Universität Bonn, Bonn, Germany, 2016).

[38] T. Takekoshi, J. Yeh and R. Knize, "Quasi-electrostatic trap for neutral atoms",
      Optics Communications **114**, 421–424 (1995).

[39] N. Masuhara et al., "Evaporative cooling of spin-polarized atomic hydrogen",
      Phys. Rev. Lett. **61**, 935–938 (1988).

[40] H. Brammer, "Ultrakalte erbiumatome in einer co_2-laser dipolfalle",
      PhD thesis (Rheinischen Friedrich-Wilhelms-Universität Bonn, Sept. 2016).

[41] M. Lewenstein et al.,
      "Ultracold atomic gases in optical lattices: mimicking condensed matter physics and beyond",
      Advances in Physics **56**, 243–379 (2007).

[42] I. Bloch, J. Dalibard and W. Zwerger, "Many-body physics with ultracold gases",
      Rev. Mod. Phys. **80**, 885–964 (2008).

[43] O. Morsch and M. Oberthaler, "Dynamics of bose-einstein condensates in optical lattices",
      Rev. Mod. Phys. **78**, 179–215 (2006).

[44] A. Van Der Ziel and E. Chenette, "Noise in solid state devices",
      Advances in Electronics and Electron Physics **46**, edited by L. Marton, 313–383 (1978).

[45] H. Kadau, "A dipolar bose-einstein condensate in a one-dimensional optical lattice",
      PhD thesis (Universität Stuttgart, Aug. 2011).

[46] H. Müller, S.-w. Chiow and S. Chu, "Atom-wave diffraction between the raman-nath and the
      bragg regime: effective rabi frequency, losses, and phase shifts", Phys. Rev. A **77**, 023609
      (2008).

[47] Y. B. Ovchinnikov et al.,
      "Diffraction of a released bose-einstein condensate by a pulsed standing light wave",
      Phys. Rev. Lett. **83**, 284–287 (1999).

[48] W. H. Bragg and W. L. Bragg, "The reflection of x-rays by crystals",
      Proc. R. Soc. Lond. A **88**, 428–438 (1913).

[49] M. Kozuma et al.,
      "Coherent splitting of bose-einstein condensed atoms with optically induced bragg diffraction",
      Phys. Rev. Lett. **82**, 871–875 (1999).

[50] C. J. Foot et al., *Atomic physics*, Vol. 7 (Oxford University Press, 2005).

[51]   P. J. Martin, B. G. Oldaker, A. H. Miklich and D. E. Pritchard,
       "Bragg scattering of atoms from a standing light wave", Phys. Rev. Lett. **60**, 515–518 (1988).

[52]   C. Cabrera-Gutiérrez et al.,
       "Robust calibration of an optical-lattice depth based on a phase shift", Phys. Rev. A **97**, 043617 (2018).

[53]   S. Friebel, C. D'Andrea, J. Walz, M. Weitz and T. W. Hänsch,
       "CO_2-laser optical lattice with cold rubidium atoms", Phys. Rev. A **57**, R20–R23 (1998).

[54]   M. Cristiani, O. Morsch, J. H. Müller, D. Ciampini and E. Arimondo,
       "Experimental properties of bose-einstein condensates in one-dimensional optical lattices:
       bloch oscillations, landau-zener tunneling, and mean-field effects", Phys. Rev. A **65**, 063612 (2002).

[55]   D. M. Giltner, R. W. McGowan and S. A. Lee, "Theoretical and experimental study of the
       bragg scattering of atoms from a standing light wave", Phys. Rev. A **52**, 3966–3972 (1995).

[56]   É. Mathieu, "Mémoire sur le mouvement vibratoire d'une membrane de forme elliptique.",
       Journal de Mathématiques Pures et Appliquées **13**, 137–203 (1868).

[57]   P. Meystre, *Atom optics*, 1st ed., Vol. 33,
       Springer Series on Atomic, Optical, and Plasma Physics (Springer-Verlag New York, 2001).

[58]   C. Keller et al., "Adiabatic following in standing-wave diffraction of atoms",
       Applied Physics B **69**, 303–309 (1999).

[59]   C. V. Raman and N. S. Nagendra Nathe,
       "The diffraction of light by high frequency sound waves: part i.",
       Proceedings of the Indian Academy of Sciences - Section A **2**, 406–412 (1935).

[60]   D. Helten, "Bragg scattering of ultracold erbium atoms off a one-dimensional optical lattice",
       MA thesis (Rheinische Friedrich-Wilhelms-Universität Bonn, Bonn, Germany, 2019).

[61]   J. E. Debs et al., "A two-state raman coupler for coherent atom optics",
       Opt. Express **17**, 2319–2325 (2009).

List of Figures

List of Tables

Acronyms

AI	absorption imaging
AOM	acousto-optic modulator
BEC	Bose-Einstein condensate
DFC	dual filament effusion cell
EC	effusion cell
HL	hot lip
MOT	magneto-optical trap
ODT	optical dipole trap
PBS	polarizing beam spliter
QUEST	Quasi-electrostatic trap
RF	radio frequency
RMS	root mean squared
TC	transversal cooling
TOF	time of flight
UHV	ultra-high vacuum
ZS	zeeman slower